Development and evaluation of precision liquid pollinator for kiwifruit

Wei Hao [a,b,c], Xinting Ding [a,b,c], Zhi He [a,b,c], Kai Li [a,b,c], Weixin Gong [a], Zixu Li [a], Zhen Yang [a], Yongjie Cui [a,b,c,*]

[a] College of Mechanical and Electronic Engineering, Northwest A&F University, Yangling, Shaanxi 712100, China
[b] Key Laboratory of Agricultural Internet of Things, Ministry of Agriculture and Rural Affairs, Yangling, Shaanxi 712100, China
[c] Shaanxi Key Laboratory of Agricultural Information Perception and Intelligent Service, Yangling, Shaanxi 712100, China

ARTICLE INFO

ABSTRACT

Cultivation of kiwifruit heavily relies on assisted pollination, and sufficient pollination can enhance fruit quality. A precision liquid pollinator for kiwifruit robotic pollination was developed as part of the research, and it was optimized with the aim of improving pollination quality while saving pollen usage. The pollinator employs a grating ruler to measure the stroke of a pneumatic hydraulic cylinder to achieve precise control of pollen suspension dosage, and uses an internal mixing air-assisted nozzles to spray pollen suspension for pollination. Through experiments of optimizing pollen suspension volume control, constructing of pollination distance prediction model, and measuring droplet size distribution, a working range of air pressure and liquid pressure was established. Eight sets of air–liquid pressure parameters were selected to evaluate the planar pollen deposition of the pollination device, and the optimal parameters were applied to pollinate kiwifruit flowers. The results indicated that reducing droplet size enhanced the overall pollen deposition rate.. In a windless laboratory environment, the developed pollinator achieved a pollen deposition efficiency of 21.15% under an air pressure of 0.15 MPa and liquid pressure of 0.25 MPa. This precision liquid pollination device is advantageous for precise control under high pressure and low flow conditions, suitable for the end effector of autonomous pollination robots. The optimization and evaluation methods established within this study provide reference for the development of precision pollination devices.

1. Introduction

Actinidia spp., a deciduous perennial vine belonging to the *Actinidia Lindl.* genus in the *Actinidiaceae* family (Li and Li, 2010), includes 54 species and 21 subspecies in the latest classification (Huang, 2016). The most widely planted varieties worldwide are the green kiwifruit (*A. deliciosa*) and the golden kiwifruit (*A. chinensis*), which are expected to continue to dominate in the future (Ferguson, 2015). By 2021, the global cultivation area of kiwifruit has reached 286,935 ha, with a yield of nearly 4,467,099 tons (UN FAO, 2021). Prior to the COVID-19 pandemic in 2019, the total global trade in kiwifruit reached $3.18 billion, accounting for approximately 2.9% of the total global fruit trade (Wu et al., 2021).

Kiwifruit is dioecious and can only produce unisexual flowers (Jerram, 1979). The lack of nectar in both staminate flowers and pistillate flowers make it difficult to attract insects for pollination (Tacconi et al., 2016). The weight of kiwifruit is closely related to the number of seeds (Castro et al., 2021; Broussard et al., 2021). Reliance on wind and insect pollination alone cannot ensure sufficient pollination (Razeto et al., 2005; Gonzalez, 1998; Pozo et al., 2018; Broussard et al., 2022), thus kiwifruit cultivation highly depends on artificial pollination.

However, manual pollination has a high labor intensity and high labor costs, also influenced by labor shortages. At the same time, kiwifruit pollen is very expensive, with an average selling price of 40,000 RMB per kilogram in Shaanxi Province, China in 2023 (sourced from online sales platforms). The amount of pollen used in the pollination process also needs to be considered for saving purposes. To address these difficulties, many auxiliary pollination technologies have been developed, some of which can be applied to robotic pollination. Chechetka et al. (2017) developed an ion liquid gel with semi-permanent adhesion properties that can simulate insect pollination. They completed contact pollination of lilies using a drone equipped with a coated pollination brush. Ohi et al. (2018) created an automatic pollination robot with a flexible TPU printed end-effector, where the brush was fixed on the TPU
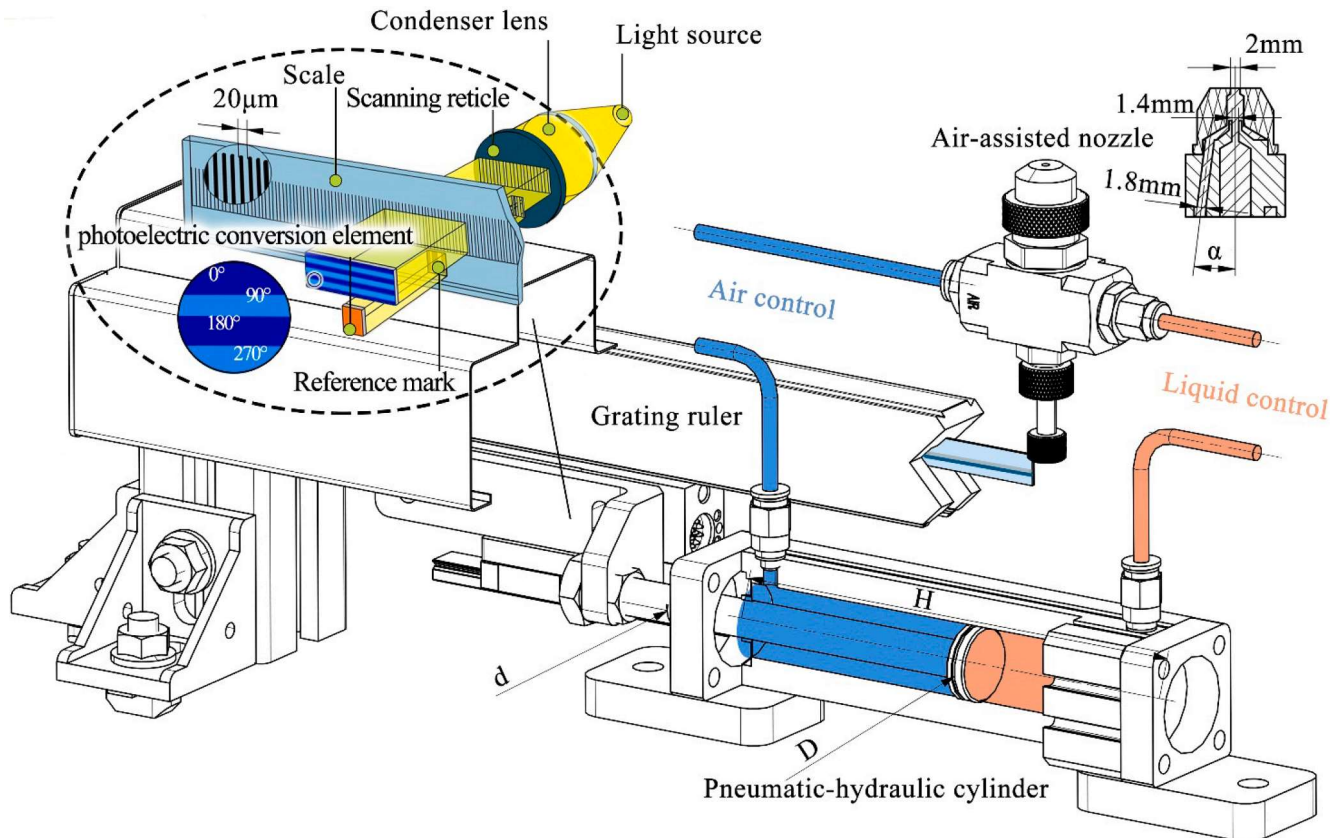

Fig. 1. Structure of the liquid precise control device for the precision liquid pollinator.

base and autonomous pollination was achieved through contact pollen transfer. Strader et al. (2019) added a servo mechanism for controlling the direction of the end effector in their pollination robot, which can achieve more accurate alignment with the flower. However, this contact transfer end effectors take a very long time to pollinate, which is inefficient and there is a risk of hitting the stigma. Yang and Miyako (2020) developed a bubble pollination device that disperses pollen in a solution and transfers it to the stigma through a bubble generator. The fruit set rate of pear pollination experiments can reach 95%. Although bubbles can effectively protect the stigma, they are susceptible to interference from outdoor winds and cannot achieve precise pollination in windy conditions. Liquid spray pollination uses an industrial nozzle to atomize pollen suspension and deliver it to the flower. Because it does not directly contact the stigma, uses less pollen and has higher accuracy, showing great potential in kiwifruit robotic pollination, but still falls short of commercial pollination requirements (Williams et al., 2019; Li et al., 2022a). Therefore, it is necessary to conduct in-depth research on liquid spray pollination to improve pollination effectiveness.

Wang et al. (2019) investigated the characteristics of internal mixing air-assisted nozzles with different forms and found that they can achieve good atomization effects at lower air–liquid pressures. Williams et al. (2021) compared the effect of external mixing air-assisted nozzles and pressure nozzles on kiwifruit pollination in a trellis planting pattern. Although the pressure nozzle resulted in slightly higher seed numbers and fruit weights, the pollen usage increased by almost two times. Shi et al. (2019) studied the control method of pollen suspension using an internal mixing air-assisted nozzle, which controlled the volume of pollen suspension by unit time on–off control. However, due to pressure fluctuations and other reasons, the volume of liquid sprayed at each time fluctuated greatly in practical use. Chang et al. (2022) studied the deposition characteristics of kiwifruit pollen during pollination using an internal mixing air-assisted nozzle, but encountered the same problem. In these studies, diaphragm pumps, gear pumps, or plunger pumps were

mainly used as liquid pressure sources. Due to structural limitations, the total amount of liquid sprayed cannot be precisely controlled under high pressure and low flow conditions. In laboratory conditions, the volume of sprayed pollen suspension is generally determined by weighing after spraying, but the experiment results are often not accurate enough due to the difficulty in collecting sprayed droplets. Although peristaltic pumps can precisely control the flow rate, they cannot be used under high pressure conditions. Moreover, for kiwifruit pollination, the required volume of pollen suspension is very small, which makes it almost impossible to control the flow rate using a liquid flow meter. The precise control of pollen suspension restricts liquid spray pollination research on kiwifruit flowers. Currently, the kiwifruit pollination evaluation system mainly focuses on field pollination. It generally uses factors like actual amount of field pollen used, fruit set rate, fruit quality, and seed quantity as evaluation indicators (Williams et al., 2019; Li, et al., 2022). However, there lacks a method that can effectively evaluate the pollination device in a laboratory setting, which also hinders kiwifruit pollination research.

A precision liquid pollinator for kiwifruit using an internal mixing air-assisted nozzle was developed in this research. The pollinator achieved precise control of the high-pressure, low-flow pollen suspension by measuring its volume using a pneumatic hydraulic cylinder with grating ruler. A pollen suspension volume control model was established, which allowed the operating range of the pollinator to be expanded. Additionally, a pollination distance prediction model was constructed at different spray pressures to enhance the accurate prediction of liquid injection range and improve pollination accuracy. The laser particle size analyzer was used to measure the diameter distribution of droplets under different pressure conditions to determine the reasonable working range. The optimal pollination parameters were determined by observing the planar deposition distribution of pollen after spraying. The UR5 robot arm combined with a depth camera was used for targeted pollination of kiwifruit flowers collected from specimens. The pollen
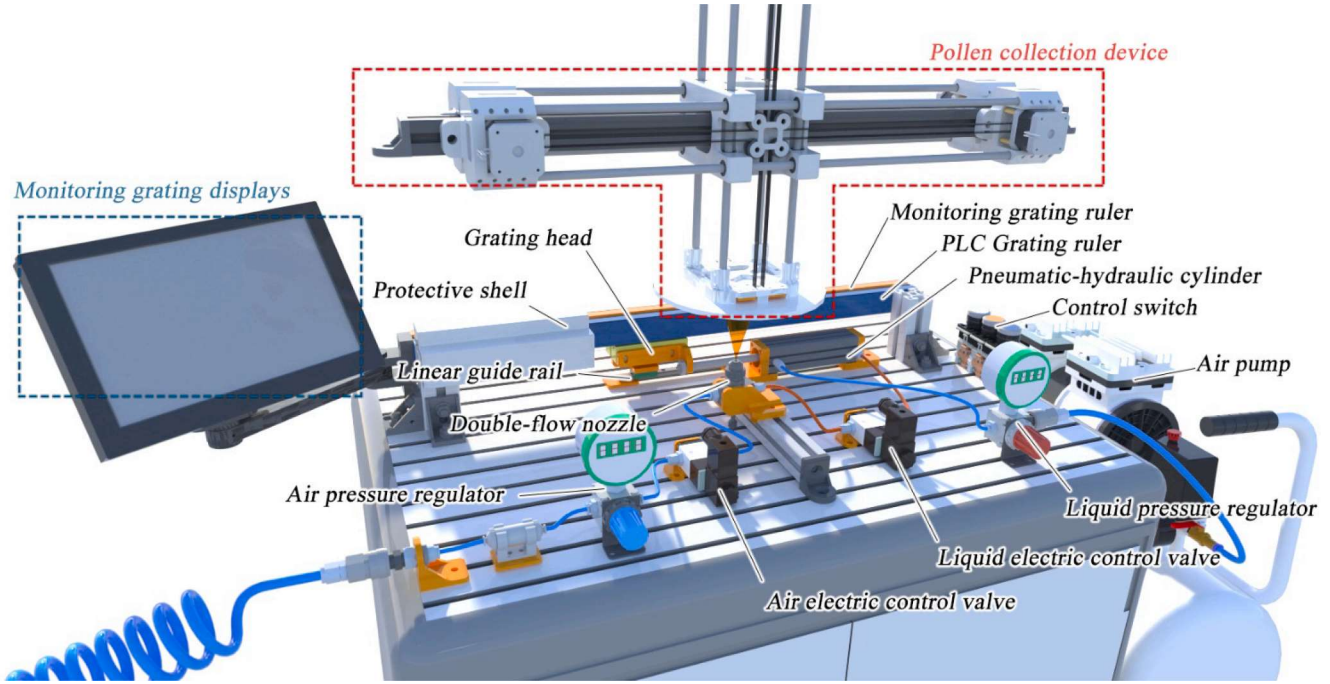
Fig. 2. Structure of the testing platform for the precision liquid pollinator.

distribution in the stigma area was analyzed to verify the optimal pollination parameters for individual kiwifruit flowers. The precision liquid pollinator developed in this study for kiwifruit has the advantages of vibration-free and high accuracy, providing technical support for kiwifruit robotic pollination.

2. Materials and methods

2.1. Construction of precision liquid pollinator

2.1.1. Mechanical structure and hardware of precision liquid pollinator

The core component of the precision liquid pollinator is the liquid precise control device, which is responsible for accurately controlling the spray volume of the pollen suspension. It mainly consists of grating measurement unit and pneumatic hydraulic cylinder execution unit, as shown in Fig. 1. The grating measurement unit includes a light source, condenser lens, scanning reticle, scale, and photoelectric conversion element. When two gratings with the same grating period overlap at a small angle, a Moiré pattern will be generated, which follows the movement of the scale. The Moiré pattern has the function of amplifying the grating distance, which enables the photoelectric element to detect changes in light intensity. The figure shows only one indicator grating, but in actual applications, four indicator gratings with a phase difference of $\pi/2$ are fabricated. equation (1) represents the signal period of the four-channel photoelectric signal. The four photoelectric elements can detect four-phase-shifted $\pi/2$ electric signals, and there is a reference mark used to output an automatic zero-setting signal. The equation (1) is given as:

$$\begin{cases} u_a = U_0 + U_m sin\dfrac{2\pi x}{W} \\ u_b = U_0 + U_m sin\left(\dfrac{2\pi x}{W} + \dfrac{\pi}{2}\right) = U_0 + U_m cos\dfrac{2\pi x}{W} \\ u_c = U_0 + U_m sin\left(\dfrac{2\pi x}{W} + \pi\right) = U_0 - U_m sin\dfrac{2\pi x}{W} \\ u_d = U_0 + U_m sin\left(\dfrac{2\pi x}{W} + \dfrac{3\pi}{2}\right) = U_0 - U_m cos\dfrac{2\pi x}{W}, \end{cases} \quad (1)$$

where W is grating pitch; x is grating displacement; U_0 is the DC voltage of the electrical signal, which corresponds to the average light intensity of the Moiré pattern; U_m is the amplitude of the electrical signal, which corresponds to the maximum change in brightness of the Moiré pattern. The AC phase and BD signals are shaped to obtain two-phase-shifted $\pi/2$ square waves.

The pneumatic hydraulic cylinder execution unit includes a blue air chamber and a red liquid chamber, and the pollen suspension is stored in the liquid chamber. The compressed air drives the middle piston, which applies pressure to the liquid chamber. By adjusting the pressure p_{a0} of the compressed air, the initial injection pressure p_l of the pollen suspension can be controlled. The injection pressure of the pollen suspension can be calculated by the following equation (2):

$$p_l = p_{a0}\left(1 - \dfrac{d^2}{D^2}\right), \quad (2)$$

where D (mm) is the diameter of the piston; d (mm) is the diameter of the piston rod; p_{a0} (MPa) and p_l (MPa) are the pressure of the air chamber and the liquid chamber.

A grating head is installed at the end of the piston rod. The photoelectric conversion element is installed inside the grating head. When the piston rod moves, it drives the grating head to move along the measurement direction. Because a 4-fold frequency is used for sampling, 4n pulses can be generated for each grating distance. When the V_l of the solution sprayed, the grating ruler emits pulses n can be calculated using the following equation (3):

$$n = \dfrac{\pi V_l W D^2}{16}, \quad (3)$$

where the distance of W is 2×10^{-2}mm; V_l (μl) is the volume of pollen suspension.

By means of a liquid control circuit and an air control circuit, the pollen suspension and compressed air are finally mixed in an air-assisted nozzle. The liquid is disturbed by the air to produce unstable fluctuations, and completes one atomization in the mixing chamber. After leaving the mixing chamber, the droplets have a speed difference from the surrounding air. After the second atomization, stable droplets wrap

Table 1
Accuracy of liquid precision pollinator testing platform.

Part name	Description	Value
monitoring grating ruler	Interval of unit raster	20 μm
PLC grating ruler	Interval of unit raster	20 μm
grating head	Frequency of pulse acquisition	4MHZ
Monitoring grating displays	Frequency of pulse reading	2MHZ
Siemens S7-200PLC	Frequency of pulse reading	2KHZ
Pollen collection device	XY axle control step distance	0.2 mm
Air pressure regulator	Pressure control accuracy	±0.01 MPa
Liquid pressure regulator	Pressure control accuracy	±0.01 MPa

the hydrated pollen and move directionally, thus completing the pollination.

To determine the optimal pollination parameters of the precision liquid pollinator and evaluate the pollination effect, a testing platform was built, as shown in Fig. 2. Based on the precision liquid pollinator, a monitoring grating ruler was added, and its grating head was connected in parallel with the grating head of the PLC grating ruler. The actual value can be read from the monitoring grating displays. A pollen collection device was installed above the air-assisted nozzle, using a core-xy structure. The movement of the pollen collection plate is controlled by two parallel 42-step motors to adjust the alignment of the nozzle and the pollination height. During the experiment, there will be a lot of liquid splashing, so a protective shell was installed on the grating ruler to protect the optical components inside.

The control accuracy of each part is shown in Table 1. The two types of grating rulers use the same detection frequency for the grating head, but different voltages are used to connect to the PLC and the monitoring grating displays, with a voltage of 24 V and 5 V, respectively. The air pressure regulator and liquid pressure regulator have the same structure, and the pressure gauge adopts a diffusion silicon pressure sensor with a pressure accuracy of ± 0.01 MPa. The constant pressure valve has an infinitely adjustable structure. In actual testing, there is significant fluctuation in the pressure gauge of the air pressure regulator when the air electric control valve is opened, so a pressure-retaining cylinder is also installed behind the air pressure regulator in actual testing to stabilize the pressure.

The hardware of the precision liquid pollinator experimental platform is shown in Fig. 3. The controller is Siemens S7-200 PLC, which reads the A and B phase pulses of the PLC grating ruler through a custom high-speed counter. The limit frequency of the counter is 2 kHz, and the working mode is 4x frequency mode. Because there is a 90-degree phase difference between the A and B phases, pulses can be captured at both rising and falling edges of each pulse, achieving a pulse capture accuracy of 5 μm. The air electric control valve and liquid electric control valve use high-speed control coils, which cannot be directly connected to the PLC output, so transistors are needed to provide additional current. Compared to electromagnetic relays, transistors can improve response speed. The controller of the pollen collection device is an ATmega328 microprocessor which drives the stepper motors through two A4988 chips.

2.1.2. Control method of precision liquid pollinator

The control method of the precision liquid pollinator is shown in Fig. 4. Firstly, the set value SV for pollen suspension volume is input into the compensation function, and the compensation model processes this input value to obtain CV. When the program start button B is pressed, the grating ruler driver program, air output port, and timer T32 are activated. When the grating ruler driver program collects AB-phase orthogonal pulses through a high-speed counter, the current count value PV is obtained. T32 is a TON (On delay timer) timer that turns on the liquid output port after completing the delay. When CV = PV, the comparator issues a reset signal and a termination signal. The grating ruler driver resets the current value PV, and the liquid control port is closed while the timer T96 is turned on. T96 is a TOF (Off-Delay Timer) timer that turns off the air output port after completing the delay. Button A can directly issue a reset signal to the grating ruler driver program to eliminate accumulated errors. Through the above program, quantitative pollen suspension injection can be achieved, and air can be turned on ahead of time and delayed to improve the atomization effect of pollen suspension.

The main control chip of the pollen collection device controller runs the GRBL open-source numerical control system. The xy-axis control can be completed by G-code, and the running trajectory of the xy-axis can be set according to needs. Because an open-loop control system is used, the
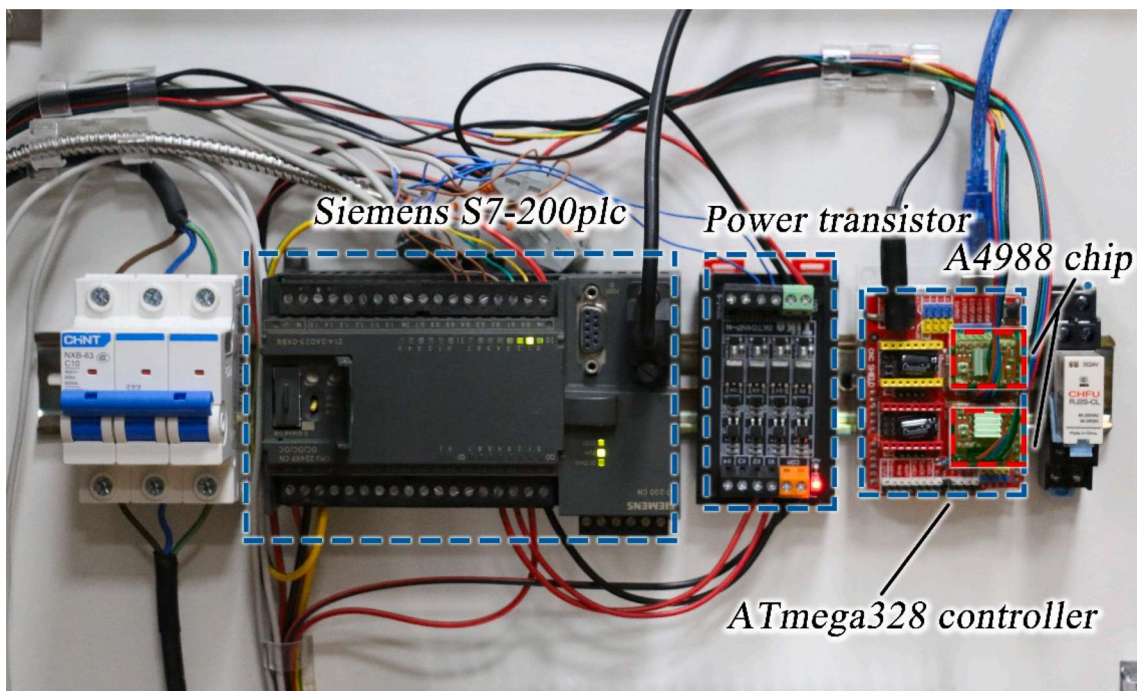
Fig. 3. Hardware of the testing platform for the precision liquid pollinator.
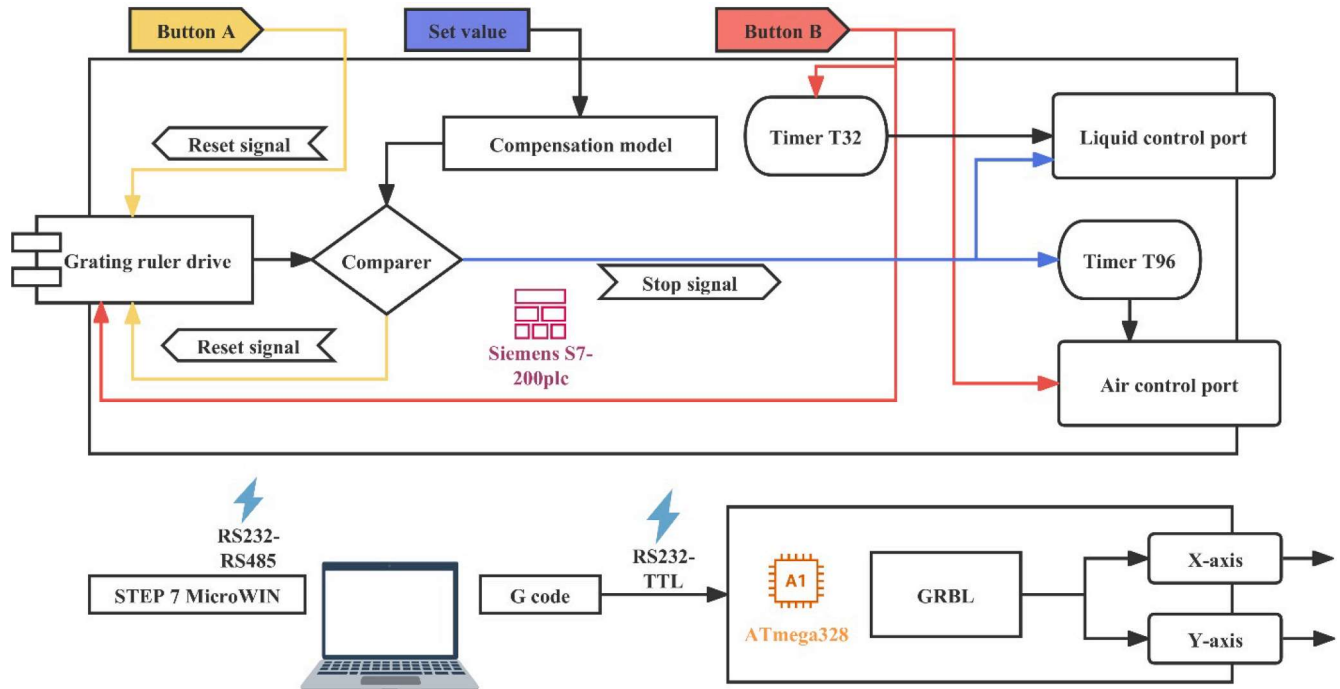
Fig. 4. Control process of the precision liquid pollinator.

Table 2
Composition of pollen suspension.

Component	Amount of substance	Weight
H_3BO_3	1.6 mM	98.93 mg
KNO_3	1.3 mM	161.76 mg
$MgSO_3 \cdot 7H2O$	0.8 mM	131.43 mg
Ca $(NO_3)_2 \cdot 4H2O$	1.8 mM	295.36 mg
Carboxymethylcellulose sodium	–	0.1 g
Xanthan gum	–	0.8 g
Kiwi pollen	–	1 g

xy-axis needs to run to the coordinate origin for calibration after power-on. After calibration is complete, the initial value of the x-axis is saved by G-code, so that the nozzle center and the pollen collection plate center can be aligned. By setting the value of the y-axis, the relative height between the pollen collection plate and the nozzle outlet can be adjusted. The advantage of doing so is that even if the pollen collection device is moved after each experiment, it can return to the position of the last experiment in the next experiment, reducing errors caused by multiple adjustments.

The S7-200PLC communicates serially with the computer through a PPI cable. The STEP7 Micro WIN running on the computer can monitor the program running status, and can also print the PV value of the grating ruler. The pollen collection device controller communicates with
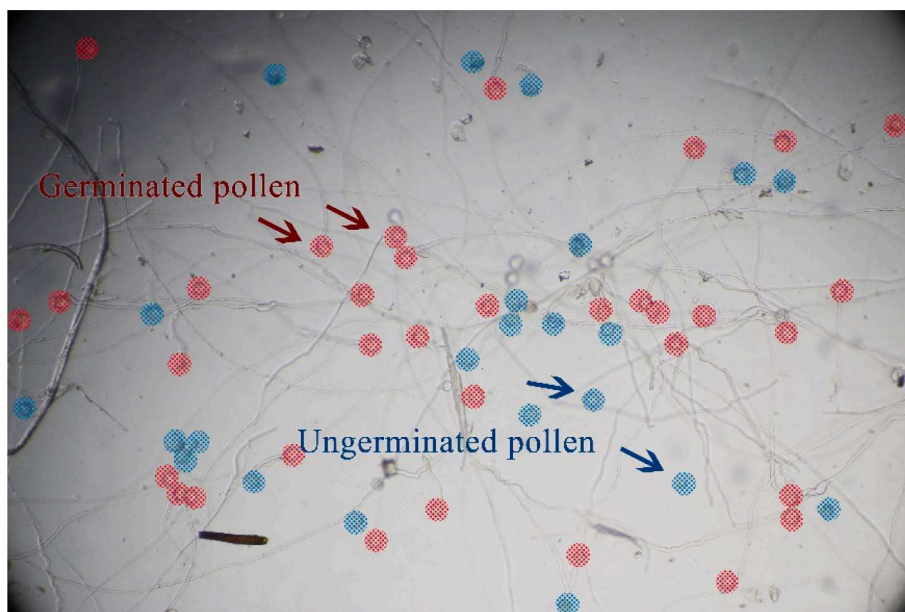

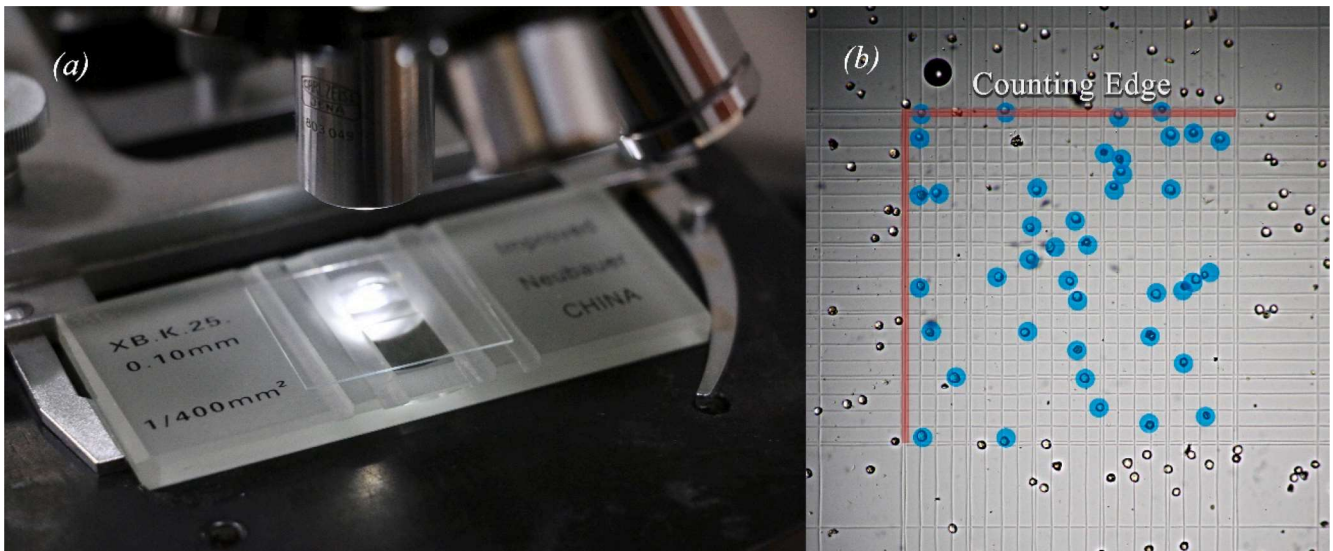Fig. 5. Kiwifruit pollen after 4 h of in vitro cultivation.

Fig. 6. Measurement of pollen concentration using a hemocytometer (a) Hemocytometer fixed on the workbench (b) Pollen on the hemocytometer.

Fig. 7. Measurement of kiwifruit flower dimensions.

the computer through an RS232-TTL converter and can directly transfer the xy-axis coordinates to the ATmega328 microprocessor using serial port commands.

2.2. Experimental materials

2.2.1. Liquid pollination suspension

The liquid pollination suspension for kiwifruit was obtained from the vitro pollen germination experiment. Pollen hydrates rapidly in a liquid environment (Fan et al., 2020), and under suitable culture conditions, the hydrated pollen will grow a pollen tube that binds to the stigma papilla cells to complete the subsequent fertilization process. Calcium ions, potassium ions and magnesium ions are consumed during pollen germination (Steinhorst and Kudla, 2013) (Cheung and Wu, 2008) (Kumari, 2022). Boron has a significant regulatory effect on pollen germination (Wang et al. 2003). Sucrose provides carbon and energy sources during pollen germination (Vasil 1987). Tushabe D and Rosbakh (2021) summarized 1572 PGM (Pollen Germination Medium) formulations from 1800 references and found that out of 100 components. Sucrose (89%), H_3BO_3 (77%), Ca^{2+} (59%), Mg^{2+} (44%), and K^+ (39%) were the most commonly used PGM components. Abreu and Oliveira (2004) obtained the highest in vitro germination rate of 86.8% for *Actinidia deliciosa* pollen using a liquid medium containing 14% sucrose, 3 mM boric acid, and 1.7 mM calcium nitrate.

The pollen suspension used in this experiment refers to the PGM components and the CBCA pollination solution proposed by Hopping and Hacking (1983), and the components per liter are shown in the Table 2. After adding pollen, air is stirred for 10 min to ensure that the pollen is fully mixed in the liquid. Sodium carboxymethyl cellulose and xanthan gum are used to improve the suspension performance of the pollen and prevent precipitation.

The pollen used was from Shaanxi Boming Pollen Co., Ltd., provided by the company for delicious kiwifruit pollen, stored in a −20 °C freezer, and its activity was restored for 6 h at 24 °C before use. After adding 14% sucrose to the pollen suspension, the pH was adjusted to 6.8 with hydrochloric acid, and the mixture was cultured on a shaker at 24 °C for 4
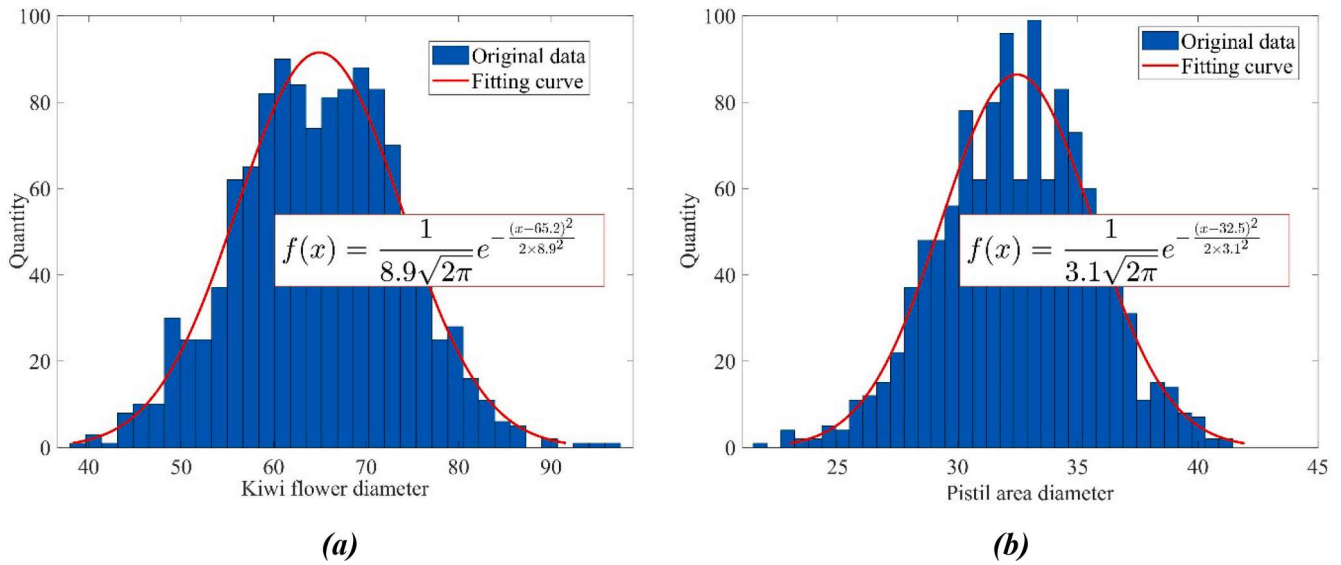
Fig. 8. Results of kiwifruit flower dimension measurements (a) Distribution of the external circle diameter of kiwifruit flowers (b) Distribution of the external circle diameter of the pistil area of kiwifruit flowers.

Fig. 9. Morphology of kiwifruit flowers after silica gel drying.

Table 3
Delay of each part of the precision liquid pollinator.

Part name	description	Delay time
Grating head	Signal acquisition period	<0.1 ms
Siemens S7-200PLC	Program scan cycle	2 ms
Power transistor	Response time	1 ms
Air pressure regulator	Action time period	10 ms
Liquid pressure regulator	Action time period	15 ms

Table 4
Basic parameters of Malvern laser particle size DP02 instrument.

Specifications of equipment	Parameters
Measuring range	1–1500 μm
Number of measurement units	48
Laser wavelength	0.6328 μm
Laser type	He-Ne
Laser power	2mW
Repeatability error	< 3%

h, resulting in a pollen germination rate of 62% (Fig. 5).

The quantity of kiwifruit pollen in liquid form was measured by conducting 50 measurements using a hemocytometer (Fig. 6).. The mean quantity of kiwifruit pollen in 0.1 mm^3 of liquid was calculated as 48 using the average error estimation method. Using formula (4), the standard deviation was estimated as σ̂ = 8.16. The formula (4) is given as:

$$\hat{\sigma} = \sqrt{\frac{\pi}{2}} \lim_{n\to\infty} \frac{\sum_{i=1}^{n} |x_i - \bar{x}|}{\sqrt{n(n-1)}}. \tag{4}$$
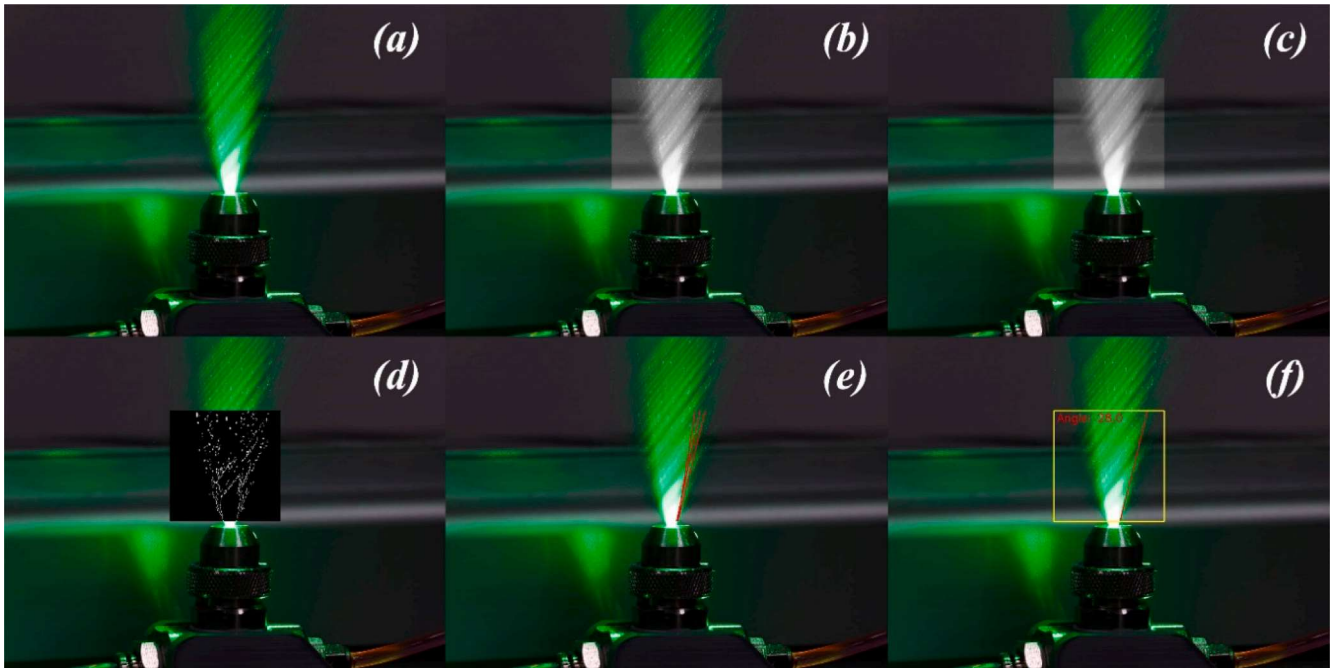
Fig. 10. Atomization angle detection using OpenCV. (a) Original image (b) Grayscale processing of the region of interest (ROI) (c) Gaussian blur processing (d) Contour extraction using the Canny operator (e) Hough transform for fog cone edge detection (f) Result plotted on the original image.

Fig. 11. Experimental setup for droplet size distribution detection.

2.2.2. Kiwifruit flowers measurement and preservation

In this experiment, it is necessary to determine the pollination parameters based on the shape and size of kiwifruit flowers, thus requiring measurements to be taken. The kiwifruit flowering period is short, with 5–6 days of concentrated blooming. In order to measure pollen distribution after pollination in a laboratory environment, kiwifruit flower specimens need to be collected and preserved.

The collection of kiwifruit flower data was carried out at the kiwifruit test station at Northwest A&F University, Mei County, Shaanxi Province, China (4°7′39″N, 107°59′50″E, 648 m above sea level). The variety planted was Hayward kiwifruit, and the planting structure used a single steel frame with two vines. The flowers and pistil area dimensions of 1200 kiwifruit flowers were measured manually and indirectly through image analysis. As shown in Fig. 7, a calibration board with a unit length of 20 mm was placed on the measurement plane for photography, and the flower dimensions were measured using ImageJ software after lens correction. The average diameter of kiwifruit flowers d_f was 65.2 mm, with a standard deviation $\sigma_f = 8.9$ mm. The measured average diameter of the pistil area d_p was $= 32.5$ mm, with a standard deviation $\sigma_p = 3.1$(Fig. 8). Therefore, to conserve pollen while ensuring pollination efficiency, the spraying range should be between d_f and d_p.

Kiwifruit flower specimens were dried directly with silica gel. The drying agent was replaced every 2 h until the drying indicator color no longer changed. The specimens were then removed and stored in a glass cover with a relative humidity below 40%. The dried kiwifruit flower specimens are shown in the Fig. 9, which allows for the preservation of
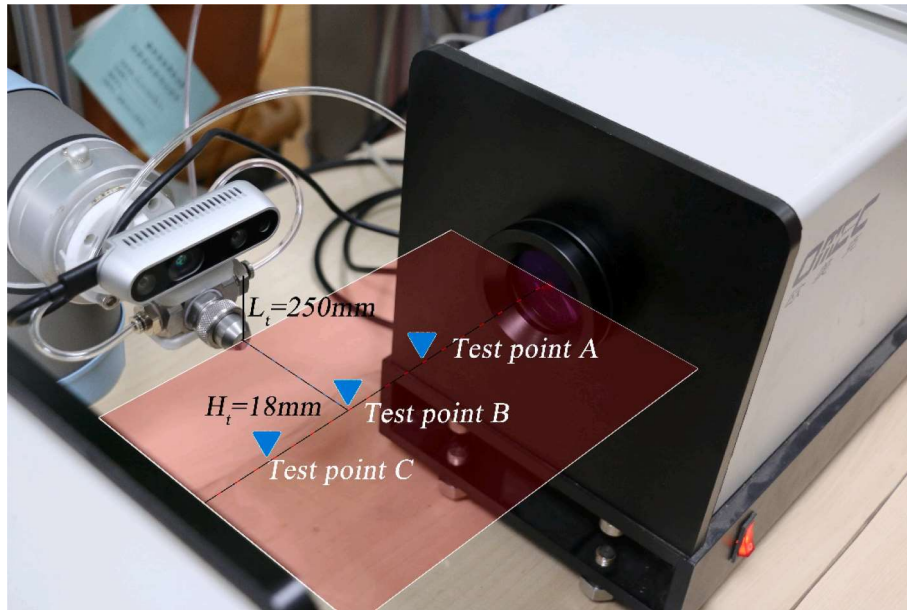
Fig. 12. Measurement points positions for droplet size distribution.
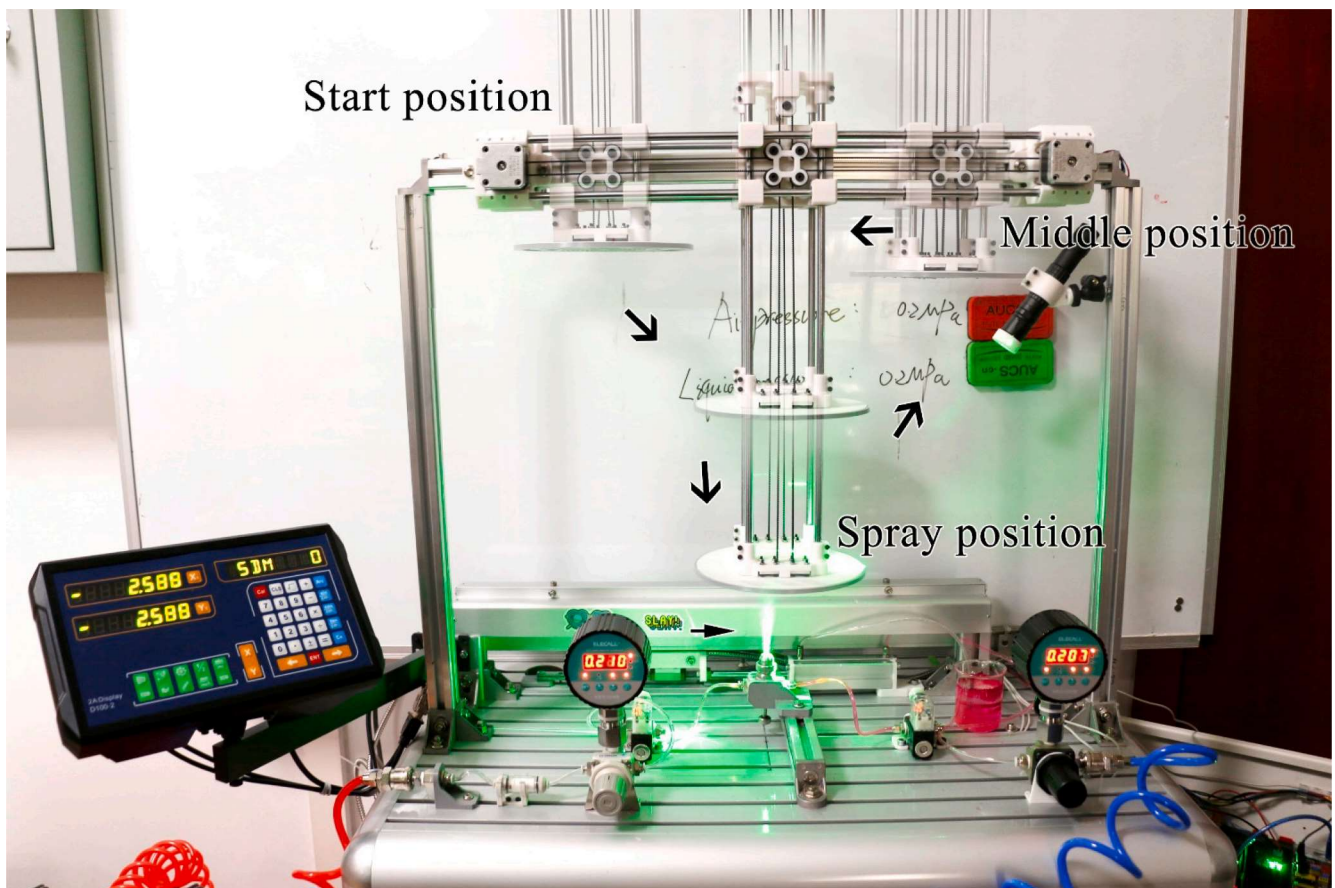

Fig. 13. Experiment process for pollen plate distribution.

the morphological characteristics of kiwifruit flowers.

2.3. Experimental method

2.3.1. Optimization of pollen suspension volume control

When the structure of the spraying system and the properties of the liquid remain unchanged, both liquid pressure and air pressure will affect the flow rate of the pollen suspension into the air-assisted nozzle. As the liquid flow rate increases, the speed of the piston movement increases accordingly. When the piston movement speed is very fast, the scanning time of the PLC and the delay of the solenoid valve will affect the control. The delay of the components is shown in Table 3. After the
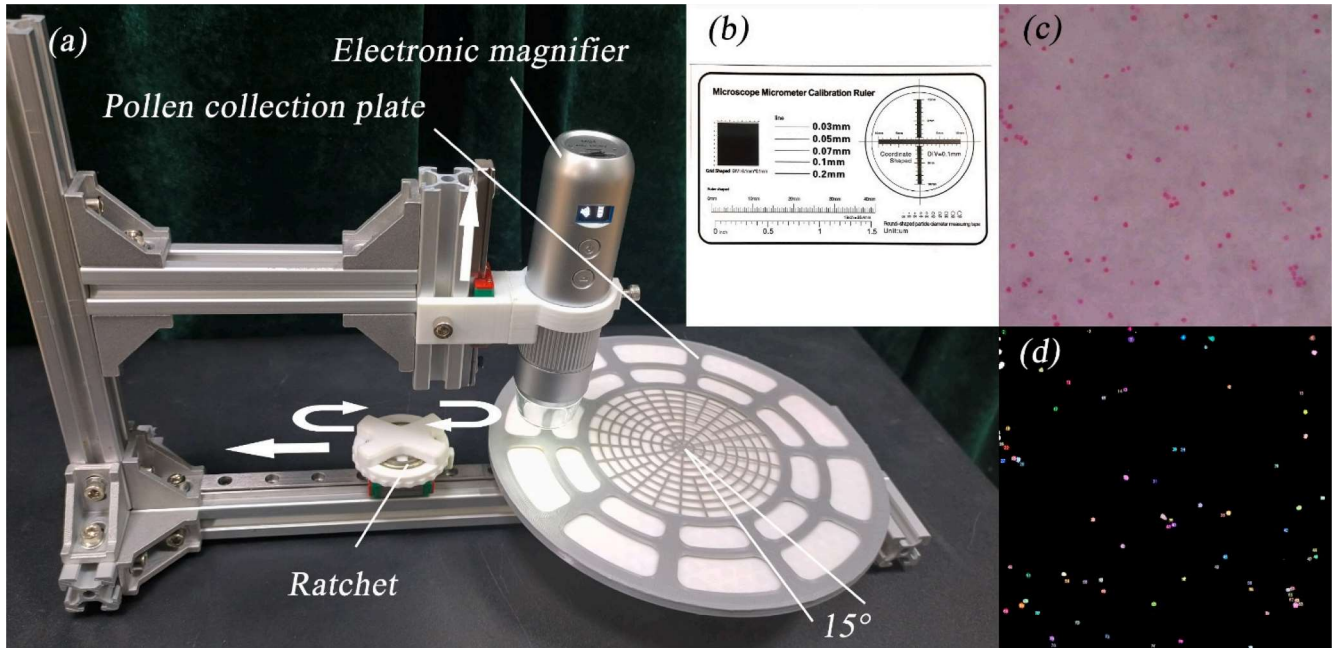
Fig. 14. Pollen image acquisition using an electronic magnifying glass. (a) Acquisition device structure (b) Microscope calibration ruler (c) Original image of pollen distribution taken (d) Counting results using Analyze Particles.
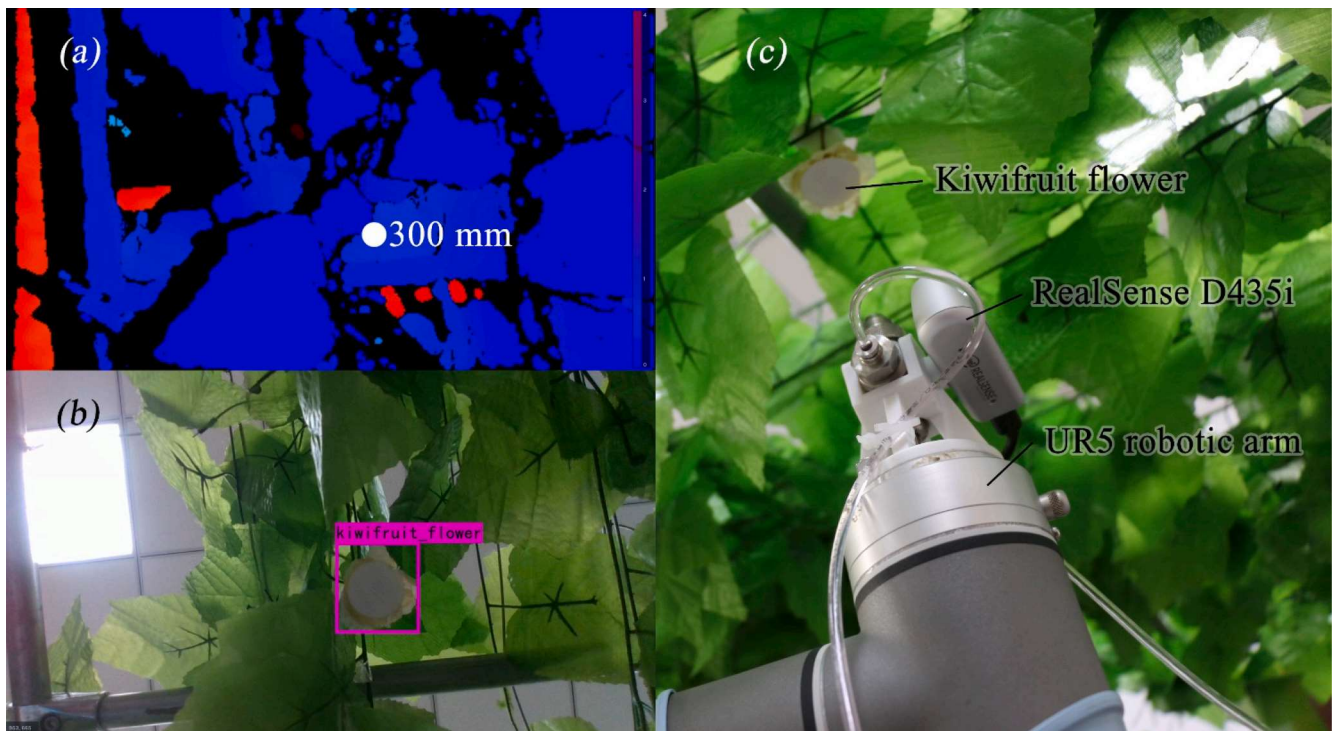

Fig. 15. Pollination verification with kiwifruit flowers. (a) Depth image captured using a depth camera (b) YoloV5 recognition result (c) Pollination using the UR5 robotic arm.

Table 5
Pulse loss measurement results.

Setting pulses	Monitor grating ruler pulses	PLC grating ruler pulses
1,000	1,133	1,129
5,000	5,134	5,131
10,000	10,099	10,104
20,000	19,752	19,755

set number of pulses is collected to send a closing signal, the piston will still move a certain distance, which will cause inaccurate pollen suspension volume. Therefore, a compensation function needs to be constructed to correct the set value. At the same time, it is necessary to avoid the system running in some intervals where no spraying can be produced or there is a large error.Table 4..

First, the experimental setup was subjected to maximum flow rate testing. The liquid pressure was set to 0.6 MPa and the air pressure was
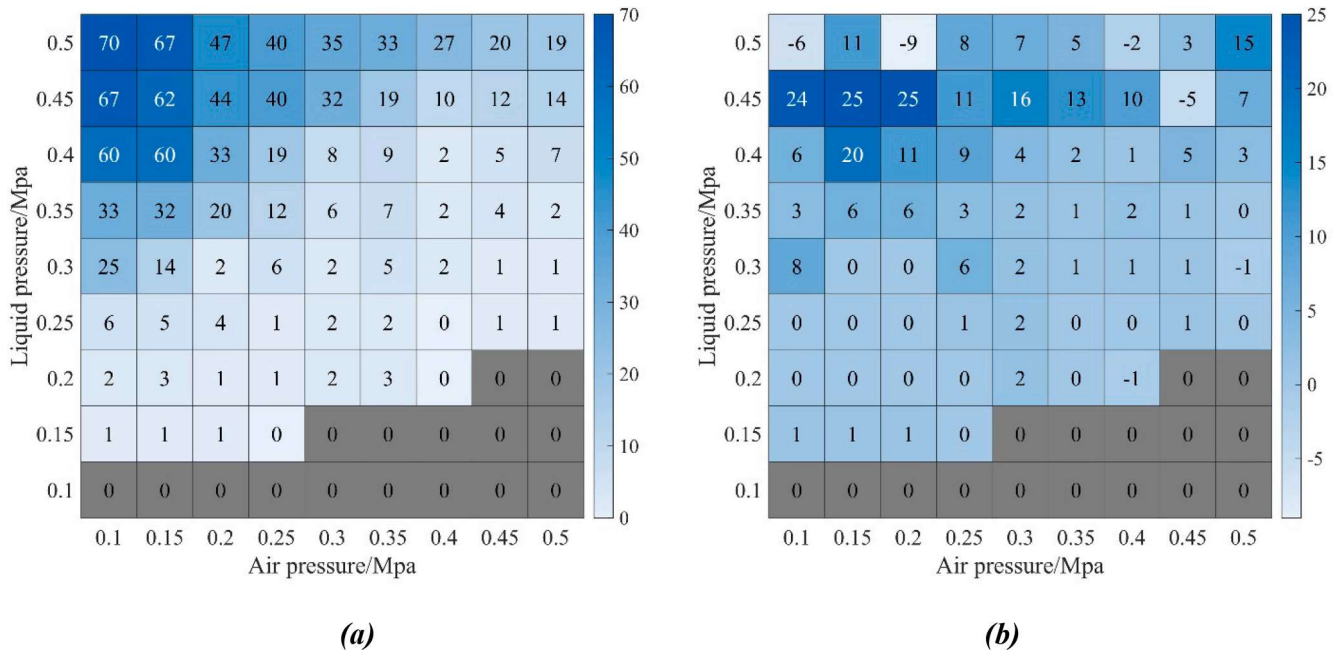
Fig. 16. Error distribution map generated under different air–liquid pressures. (a) Error distribution without error compensation (b) Error distribution after error compensation.
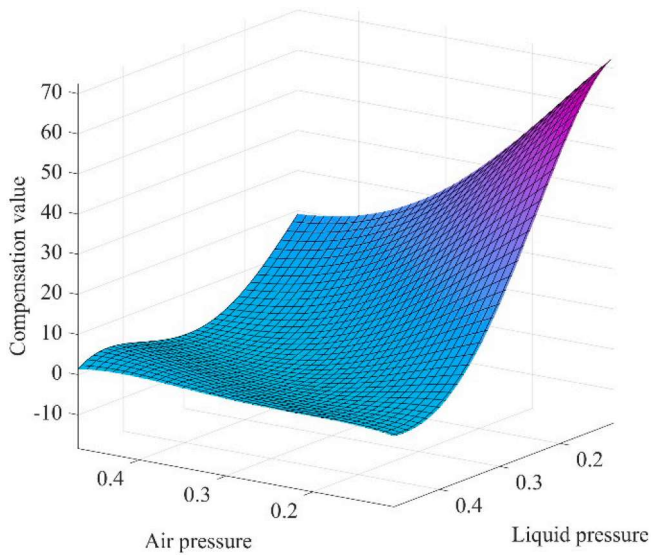
Fig. 17. Fourth-degree polynomial error compensation model.

set to 0, so that the liquid was not affected by air resistance and the maximum flow rate was obtained. The number of pulses captured by the monitoring grating ruler and the PLC grating ruler were compared to detect whether pulse loss occurred. Next, the air pressure and liquid pressure were set at intervals of 0.05 MPa from 0.1 MPa to 0.5 MPa, and the error value and non-working interval were measured. A heatmap was drawn, and then the air–liquid pressure values and error values were imported into Matlab for fitting to obtain the compensation function. Finally, the liquid control accuracy of the system loaded with the compensation function was tested.

2.3.2. Construction of the pollination distance prediction model

During the pollination process, it is necessary to control the range of pollen suspension injection, and the injection of pollen suspension should be concentrated in the stigma area as much as possible. Moreover, the pollen should be uniformly distributed in the stigma area to increase the success rate of pollination. The air-assisted nozzle has a misting angle that changes with the variation of the spray pressure. The misting angle is influenced by both liquid pressure and air pressure, so it is necessary to establish the relationship between spray pressure and misting angle. By adjusting the liquid pressure and air pressure and projecting a laser beam onto the spray plane through a spectrophotometer, the liquid control signal is connected to an electromagnetic

Table 6
Atomization angle under different air–liquid pressures.

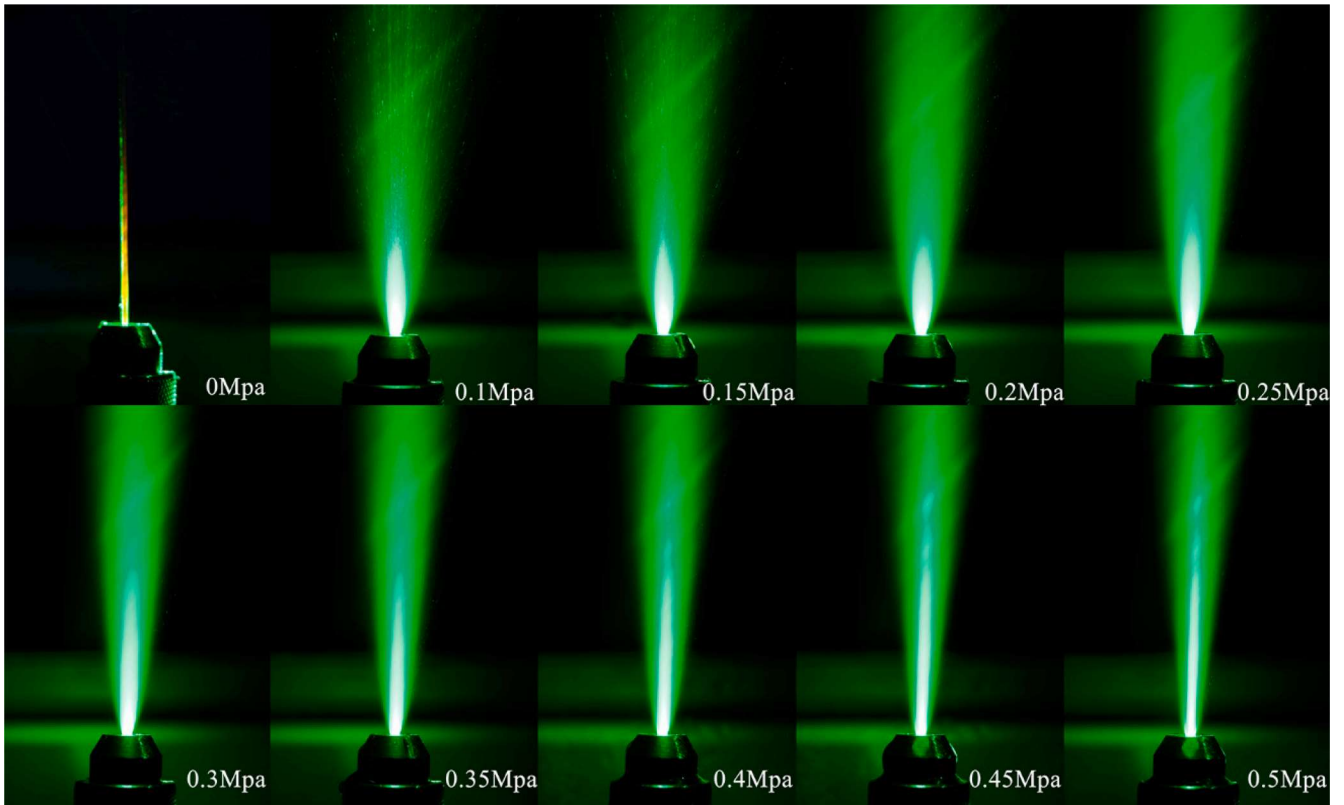| Liquid pressure /Mpa	Air pressure /MPa									
	0	0.1	0.15	0.2	0.25	0.3	0.35	0.4	0.45	0.5
	Spray angle /(°)									
0	0.00	0.00	0.00	0.00	0.00	0.00	0.00	0.00	0.00	0.00
0.1	0.00	0.00	0.00	0.00	0.00	0.00	0.00	0.00	0.00	0.00
0.15	0.00	0.00	0.00	0.00	0.00	0.00	0.00	0.00	0.00	0.00
0.2	0.00	29.60	19.96	16.40	15.72	13.27	12.71	0.00	0.00	0.00
0.25	0.00	30.73	26.25	18.41	17.58	14.56	14.86	14.32	14.01	13.72
0.3	0.00	31.22	27.15	24.50	21.54	18.40	17.25	16.75	15.74	14.25
0.35	0.00	32.50	28.09	25.80	22.94	20.75	20.53	18.36	15.83	16.02
0.4	0.00	33.03	29.12	27.78	23.83	22.62	21.44	19.63	18.86	16.45
0.45	0.00	33.33	29.39	27.43	24.66	24.20	24.20	22.63	19.84	19.48
0.5	0.00	34.15	30.01	28.65	26.01	25.97	24.96	22.95	20.15	19.57

Fig. 18. Atomization angle image when the liquid pressure is 0.3 MPa.
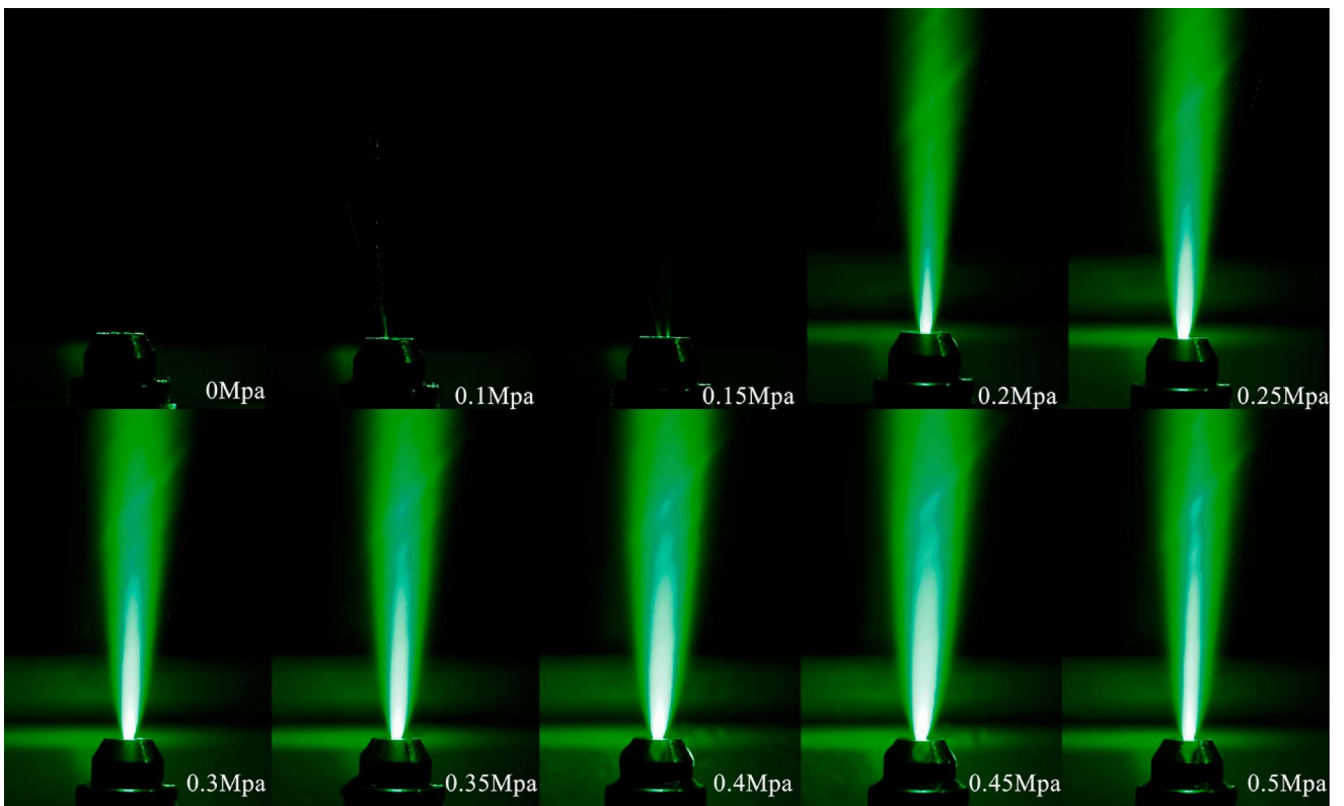

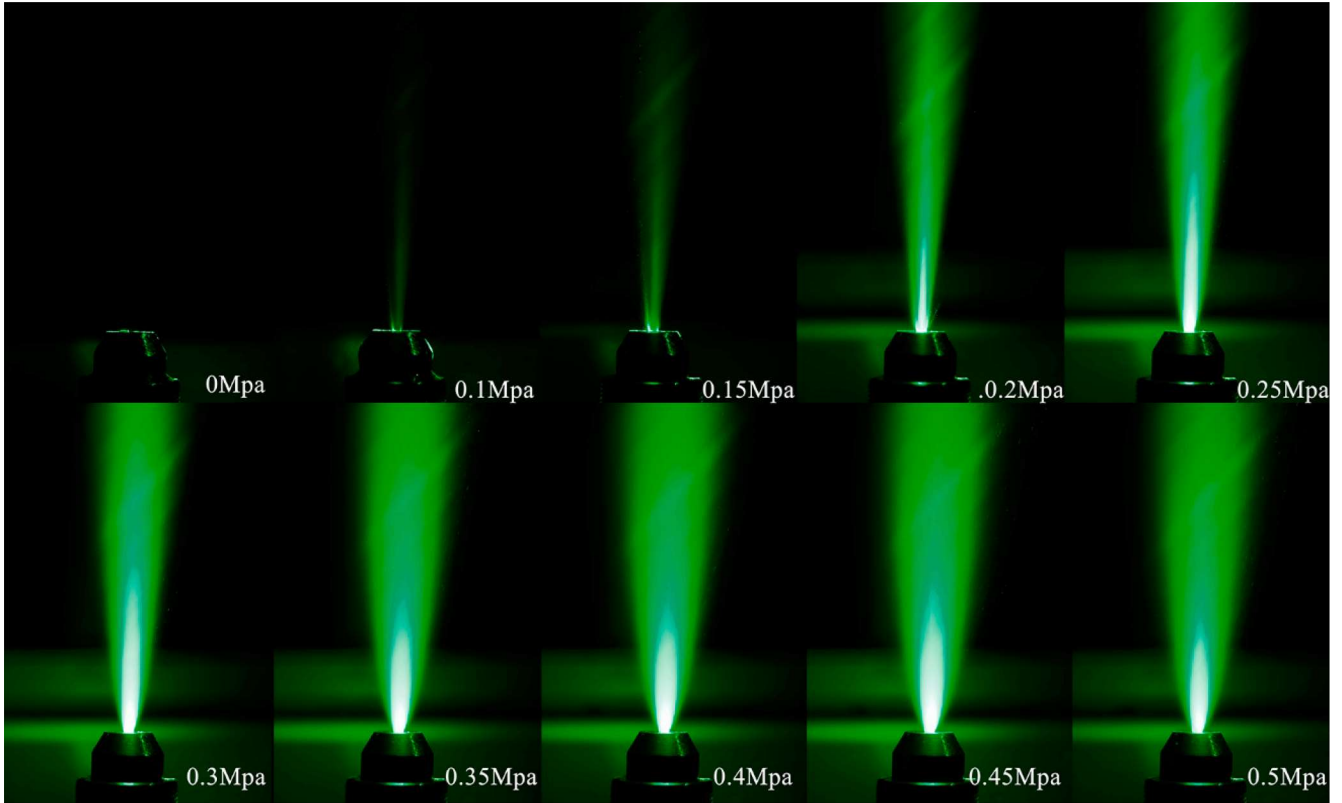**Fig. 19.** Atomization angle image when the air pressure is 0.3 MPa.

Fig. 20. Atomization angle image under equal air–liquid pressure conditions.

Table 7
Goodness-of-fit and fitting results of spray angle prediction validation.

Goodness of Fit					Goodness of Verify	
SSE	R2	Adjusted R^2	RMSE		SSE	RMSE
90.81	0.9558	0.9517	1.297		5.5176	0.9505

valve, and a Canon 70D camera is connected via a shutter line for 0.5 s of long exposure photography after each spray. The obtained images are processed using the OpenCV-Python function library to obtain the misting angle. The main processing steps are shown in Fig. 10. First, an ROI (Region of Interest) area near the root of the spray torch is drawn. After the obtained images are processed by grayscale processing and Gaussian blur processing, the contour is extracted using the Canny operator, and the edge detection of the spray cone is determined using the Hough transform and drawn on the original image. If multiple edges are detected, the average angle is taken. Assuming that the spray torch can maintain a cone shape within a certain range, the pollination distance h can be calculated using equation (5) based on the misting angle θ and the diameter of the outer circle of the target area D_a. The equation (5) is given as:

$$h = \frac{D_a}{2 tan\left(\frac{\theta}{2}\right)}. \tag{5}$$

2.3.3. Measurement of droplet size distribution

The pollen suspension volume control model and the pollination distance prediction model were established in the previous two sections. By combining equation (2) with the pollen suspension volume control model, the volume of pollen suspension sprayed each time can be determined. Next, the spraying parameters for the liquid and air are determined. Typically, the droplet diameter produced by an air-assisted nozzle is determined by multiple factors, mainly influenced by liquid flow rate, air flow rate, air–liquid ratio, liquid properties, and nozzle structure. Due to the complexity and interactions of these factors, it is difficult to provide a universal formula to calculate the droplet diameter of an air-assisted atomizer. Generally, the droplet diameter of an air-assisted atomizer is estimated through experimentation and empirical formulas. Wang et al. (2022) studied the droplet distribution characteristics of air-assisted atomizers and obtained the results of the droplet distribution changing with air pressure and liquid pressure through experiments with pure water. Under room temperature conditions of 20°C, the surface tension coefficient of pollen suspension was measured to be 72.6 dyn/cm, the liquid dynamic viscosity was 0.09 dyne·s/cm^2, and the density was 1.0 g/cm^3, which is similar to the properties of pure water. Therefore, in the scope of this research, the expected droplet diameter distribution can be directly determined through liquid pressure and air pressure.The air-assisted nozzle's droplet diameter distribution was measured using the DP02 laser particle size analyzer from Malvern Instruments. The instrument parameters are shown in Table 4, and 48 measurement units were used to detect characteristic diameters in the range of 1–1500 μm. The experimental environment was set up as shown in Fig. 11, and the internal mixing air-assisted nozzle was installed on the end of a UR5 robot arm using a bracket. The air pressure and liquid pressure were regulated within the range of 0–0.5 MPa by means of a precise pollination testing platform. In this experiment, a multi-modal distribution was used for data statistics instead of the Rosin-Rammler distribution traditionally used for particle size diameter statistics. Since droplets do not have a characteristic size, the influence of environmental particles on the measurement was first removed by sampling the background light before measurement. The measurement position is shown in Fig. 12, and equation (5) is used to estimate the detection position. Here, D_a is determined by the average diameter of the kiwi flower and stigma area equation (6). The measurement distance L_t is 250 mm, and the spacing between the three measurement points is 18 mm. The equation (6) is given as:
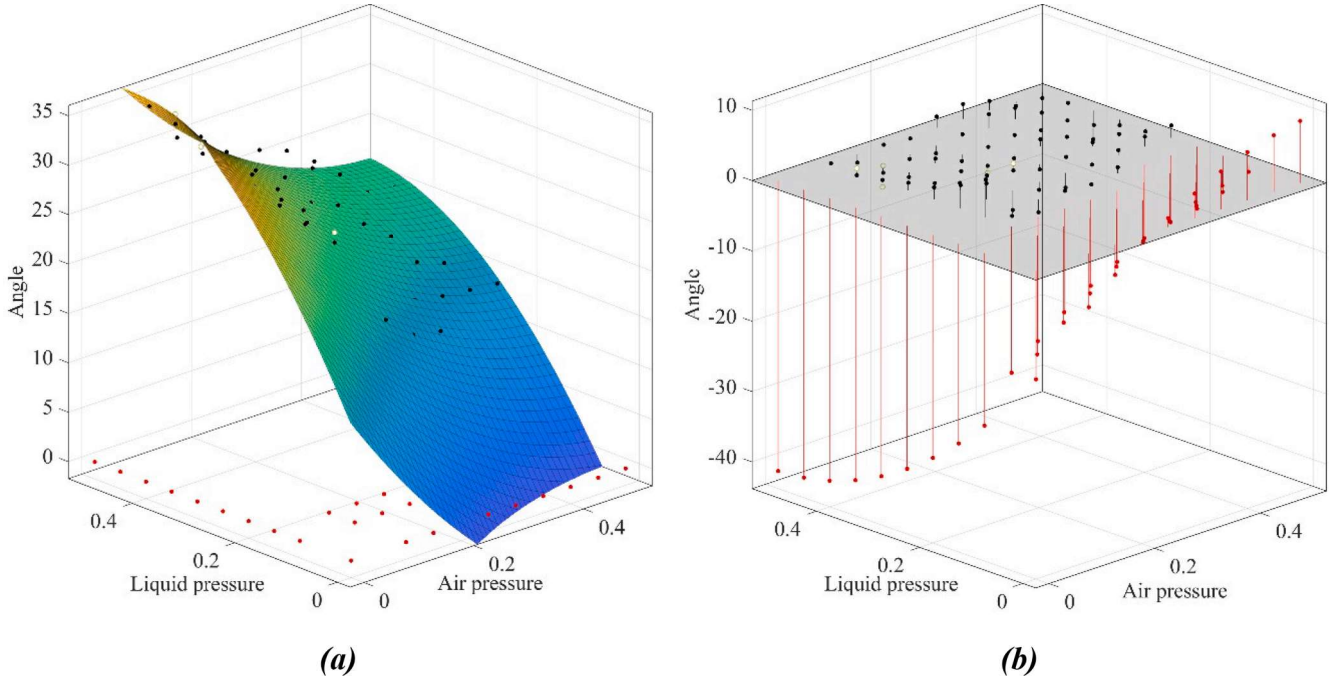
Fig. 21. Atomization angle prediction model. (a) Results obtained by quadratic polynomial fitting (b) Residual distribution.

$$D_a = \frac{(d_f + \sigma_f) + (d_p + \sigma_p)}{2}. \qquad (6)$$

The PalDat - Palynology database shows that kiwi pollen, when fixed in a hydrated state using the DMP method, is approximately spherical with an equatorial polar axis of approximately 25 μm (Halbritter, 2016). Therefore, while ensuring atomization efficiency, the diameter of sprayed droplets should be avoided to be smaller than 25 μm to prevent pollen from losing its coating and being damaged. D_{25} was used as the criterion for particle diameter distribution in this experiment, as indicated by equation (7). When 25% of the particles had a diameter smaller than 25 μm, there was considered to be a risk of pollen damage. The equation (7) is given as:

$$D_{25} = \frac{\sum_{i=1}^{n} d_i F_i - F_{\frac{1}{2}} d_{\frac{1}{2}}}{F_{\frac{1}{2}} - F_{\frac{1}{4}}}, \qquad (7)$$

where n represents the number of particles in the sample, d_i denotes the size of the ith particle, and F_i represents the cumulative distribution function (CDF), which is the proportion of particles that are smaller than or equal to d_i. $F_{\frac{1}{2}}$ represents the size of the particle at the 50th percentile, or the median particle size, while $F_{\frac{1}{4}}$ represents the size of the particle at the 25th percentile.

2.3.4. Measurement of pollen plane deposition distribution

Using pollen suspension volume control model and pollination distance prediction model, combined with the mist droplet size distribution range, a planar kiwifruit flower deposition experiment was conducted.

For Hayward (delicious kiwifruit), a minimum of 10,600–13,250 pollen grains adhering to the stigma is required for full pollination, according to Broussard et al(2021). In this research, the minimum pollen volume was estimated to be approximately 33 μl using a pollen suspension with a minimum pollen concentration of 40 grains per 0.1 μl. However, in actual kiwifruit growth, stigmas are sparsely distributed in the pistil area, and a large amount of pollen adheres to the style. Considering that the theoretical deposition area is larger than the pistil area, and the distribution of stigmas in the pistil area is not uniform, the actual amount of pollen suspension used will be greater than the minimum. Chang et al. (2022) found a maximum pollen deposition rate of

10.1% using liquid pollination. Therefore, for pollen deposition experiments, the amount of pollen suspension used needs to be increased, and within the context of this study, V_l was set to be $10V_{min}$. The pollen deposition rate η in the pistil area was calculated as the ratio of the total number of pollen grains sprayed in a single application to the number of pollen grains deposited in the measurement area of 1 mm². The equation (8) used was:

$$\eta = \frac{\sum_{m=1}^{149} S_m \cdot n_m}{V_l \cdot C}, \qquad (8)$$

where S_m is the area of the measurement region, n_m is the number of pollen grains deposited in 1 mm² of the measurement area, and C is the number of pollen grains in 1 μl, which was 400 in the scope of this research, assuming a uniform distribution of pollen grains in each measurement region.

Before the measurement, a reasonable air–liquid pressure value is selected in the mist droplet size distribution range, and the spray angle is calculated according to the air–liquid pressure value. The pollination area diameter is set according to equation (6), the pollination distance is calculated according to equation (5), and the pollen suspension volume is converted into pulses according to equation (3) and transformed into actual pulses through the pollen suspension volume control model.

Measurement process is shown in Fig. 13. Air pressure and liquid pressure are adjusted, and the pollen collection plate moves from the initial position to the set position. The precision pollination system is activated and the aerosolized pollen suspension is collected by the pollen collection plate. The detection method is shown in Fig. 14. After removing the pollen collection plate, it is installed on the counting platform. The counting platform has a ratchet that can fix the pollen collection plate and achieve a unit angle rotation of 15°. Data collection is carried out for 149 areas using an electronic magnifying glass. The camera is calibrated using a microscope calibration ruler, and the collected pollen images are cropped to 1 mm² according to the calibration results. The segmented image is binarized and analyzed using the watershed algorithm in ImageJ's Analyze Particles function. The data is stored in polar coordinates. To better detect pollen distribution, Eosin was added as a dye to the pollen suspension used in this experiment, making the pollen appear red.
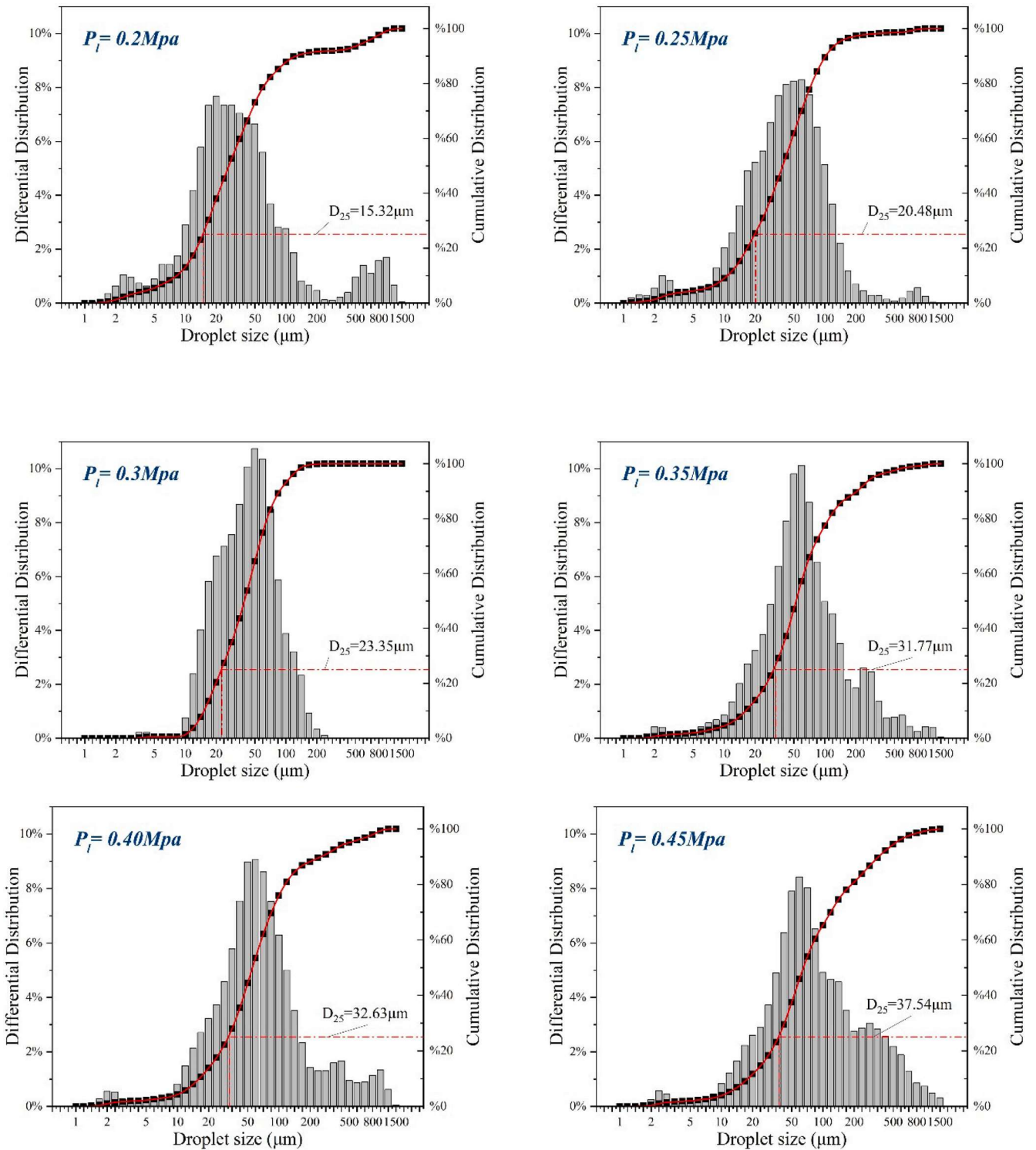
Fig. 22. Fog droplet size distribution when the air pressure is 0.3 MPa.

2.3.5. Kiwifruit pollination verification

A standard planting frame was set up in the laboratory environment, and collected kiwifruit flower specimens were fixed to the frame. The stamen region was covered with printing material with a diameter of d_p. The precision liquid pollinator was mounted on a UR5 robotic arm. The RealSense D435i depth camera was used to capture RGB and depth images to achieve automatic pollination.

Before conducting the verification, the end of the robotic arm and the camera were calibrated. Six ping pong balls were uniformly placed in

space as markers. The RealSense SDK calibration tool was used to capture the three-dimensional coordinates of the markers. The coordinate origin of the robotic arm end effector was moved to the marker position, and the position and posture of the robotic arm were recorded using the Base Link. The calibrateHandEye function in the OpenCV library was used to calculate the transformation matrix between the camera and the robotic arm end effector, completing the hand-eye calibration. Due to the 200 mm depth blind zone of the depth camera, image capture was performed at a distance of approximately 300 mm from the bottom of
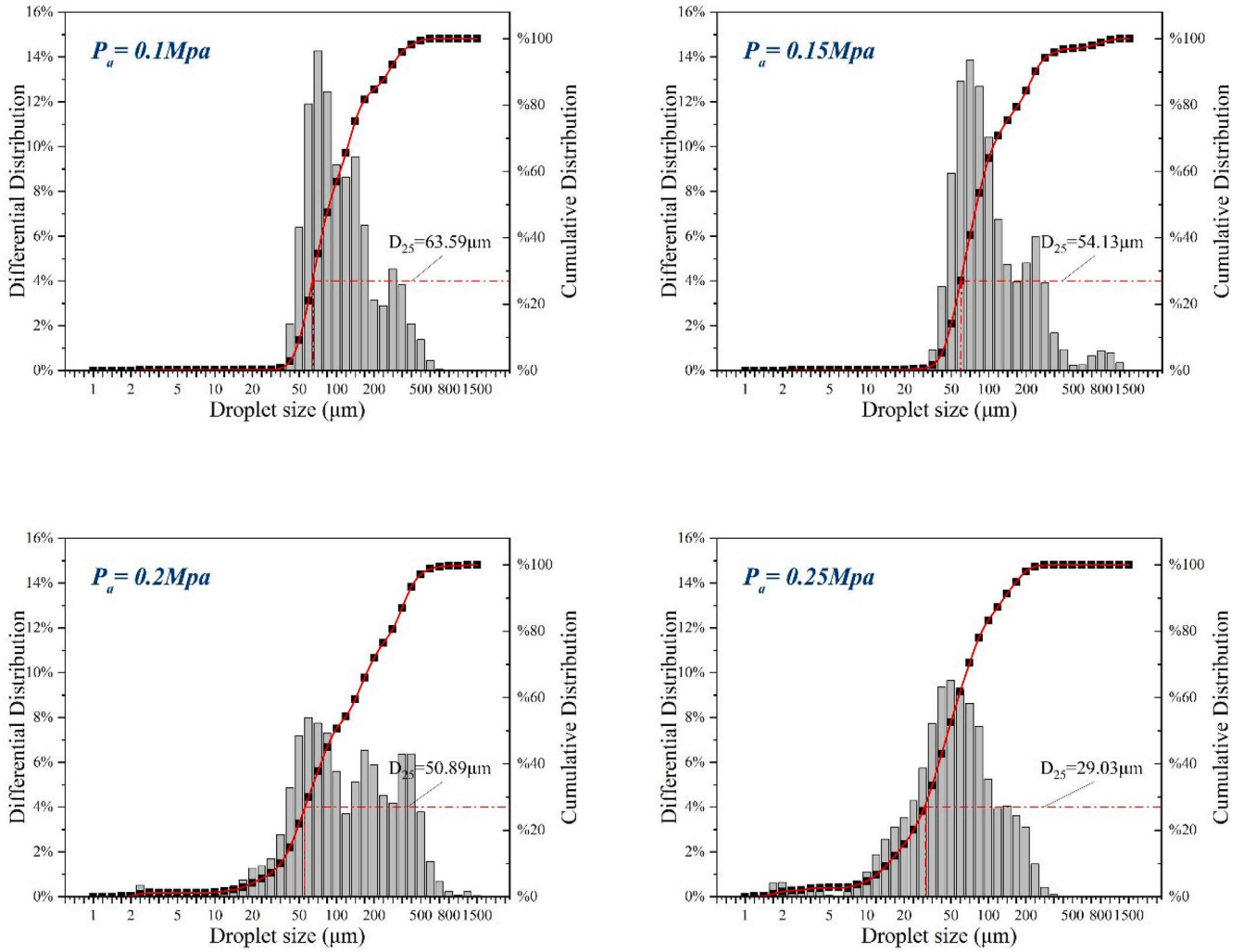
Fig. 23. Fog droplet size distribution when the liquid pressure is 0.3 MPa.

the canopy layer, and the canopy was traversed according to the camera's field of view.

In a previous study, kiwifruit flowers were recognized using the YOLOv4 model with an accuracy of 95.27% (Li et al., 2022b). The output circle center coordinates and depth values of the center point in the depth image were used as the spatial position of the kiwifruit flowers. Because kiwifruit flowers mostly grow vertically downward, the vector of kiwifruit flowers was defined as vertical downward. Based on the established pollination distance prediction model, the spatial coordinate vector with the nozzle center as the origin was calculated. After the UR5 aligned the kiwifruit flower, spraying pollination was carried out, and the pollen deposition distribution in the stamen region of kiwifruit flowers was recorded (Fig. 15).

3. Results and discussion

3.1. Pollen suspension volume control model

In the extreme flow rate test, the comparison of the number of pulses captured by the monitoring grating ruler and the PLC grating ruler is shown in Table 5. When the set pulse is less than 20,000 pulses, the number of pulses collected by both grating rulers exceeds the set value, and the main reason for this error is the hardware delay. When the set value is 20,000, the results are all less than 20,000, and the main reason

for this problem is that the limit stroke of the pneumatic hydraulic cylinder is reached. The difference in each measurement result is less than 5, and the sampling frequency of the monitoring grating ruler is 10 times that of the PLC grating ruler, so it can be considered that there is no problem of pulse loss due to insufficient monitoring frequency in this experiment.

Fig. 16(a) shows the error distribution chart generated at different air–liquid pressures, where the gray area represents the non-working interval of the device, in which the pollen suspension flow is 0 or extremely small and cannot be applied in practice, so these intervals are excluded. When the liquid pressure is constant, the error will gradually decrease as the air pressure increases. The main reason is that higher air pressure will produce reverse pressure on the liquid, thereby reducing the flow rate of the liquid, and the effect of hardware delay will be significantly reduced. Similarly, when the air pressure is constant, the error will gradually increase as the liquid pressure increases. From the graph, it can be seen that when the air pressure is 0.1Mpa and the liquid pressure is 0.5Mpa, the maximum error of 70 will be produced. The collected error values are fitted with a fourth-order polynomial and the results are plotted in a three-dimensional coordinate system as shown in Fig. 17, with R^2 is 0.964. The error distribution chart after compensation is shown in Fig. 16(b), where it can be seen that the accurate working interval has been expanded and the error values throughout the entire interval have been reduced. However, negative values also appear on
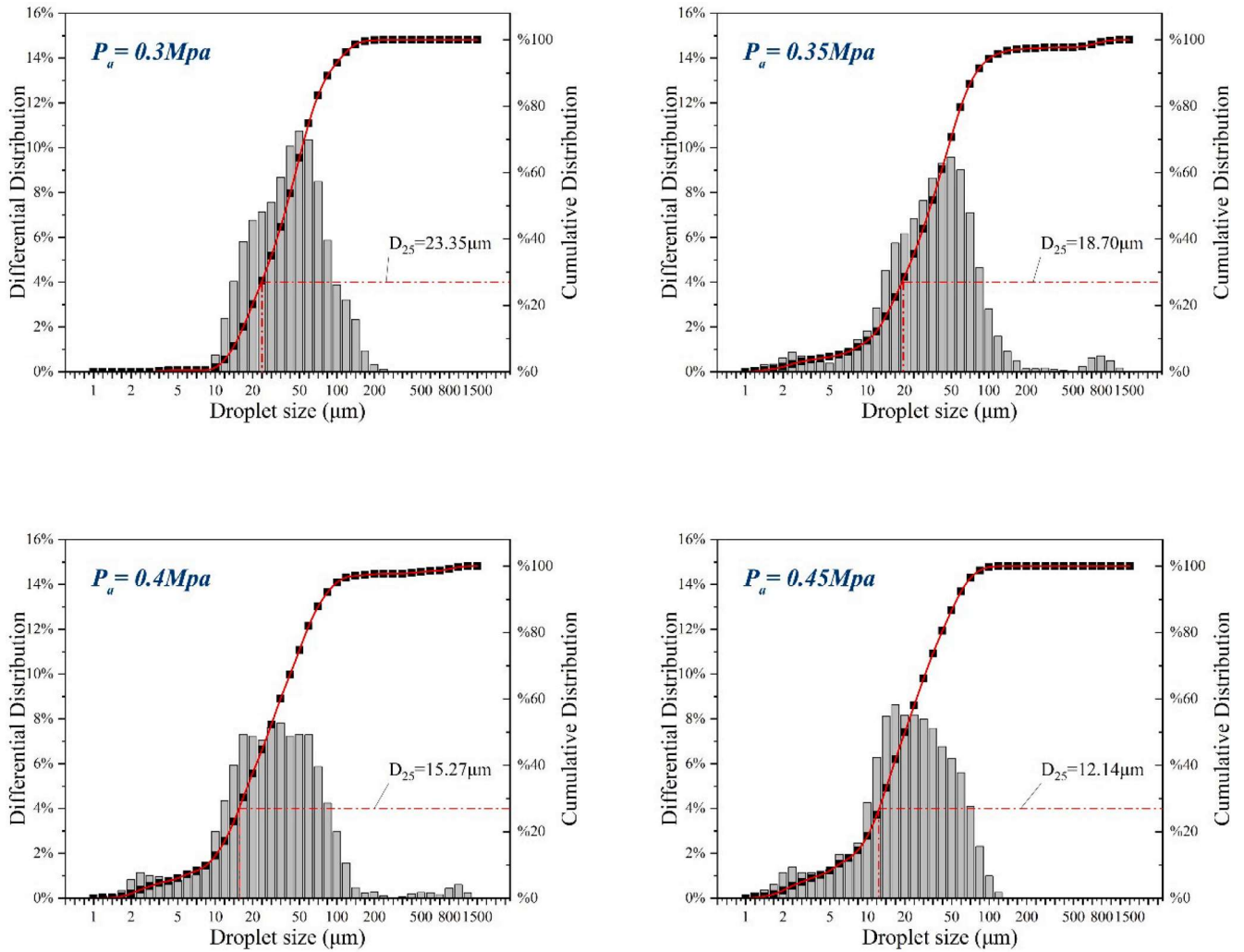
Fig. 23. (*continued*).

Table 8
D_{25} under different air–liquid pressures.

Liquid pressure /Mpa	Air pressure /MPa									
	0	0.1	0.15	0.2	0.25	0.3	0.35	0.4	0.45	0.5
	D_{25} /(μm)									
0	0.00	0.00	0.00	0.00	0.00	0.00	0.00	0.00	0.00	0.00
0.1	0.00	0.00	0.00	0.00	0.00	0.00	0.00	0.00	0.00	0.00
0.15	0.00	0.00	0.00	0.00	0.00	0.00	0.00	0.00	0.00	0.00
0.2	0.00	61.56	52.68	40.89	18.75	15.32	12.31	0.00	0.00	0.00
0.25	0.00	63.57	53.21	43.77	22.50	20.48	15.23	13.55	12.20	12.02
0.3	0.00	63.59	54.13	50.89	29.03	23.35	18.70	15.27	12.14	12.18
0.35	0.00	61.38	61.17	54.91	35.25	31.77	24.40	23.26	12.35	13.41
0.4	0.00	75.06	74.22	55.49	27.07	32.63	25.12	24.90	20.86	15.35
0.45	0.00	76.49	74.78	55.61	37.67	37.54	26.32	25.88	22.82	15.83
0.5	0.00	84.25	82.14	58.64	38.26	37.17	28.34	26.10	23.70	17.65

the graph, which is caused by excessive compensation. Moreover, under higher liquid pressure, the error compensation is not stable enough, and larger deviations will still occur. Therefore, these ranges should be avoided as much as possible during the working process. The study defines a stable operating range limit of 3 pulses, calculated to be within a liquid control error of ± 4.7 μl.

3.2. Pollination distance prediction model

The results of the atomization angle measurements are shown in Table 6. Changes of air and liquid pressure can affect the size of the atomization angle. When the liquid pressure is less than or equal to 0.15 MPa, no atomization angle can be formed, or the atomization angle is not obvious. The maximum atomization angle of 34.15° is achieved at a liquid pressure of 0.5 MPa and a air pressure of 0.1 MPa. Fig. 18 shows the atomization angle image collected under a constant liquid pressure
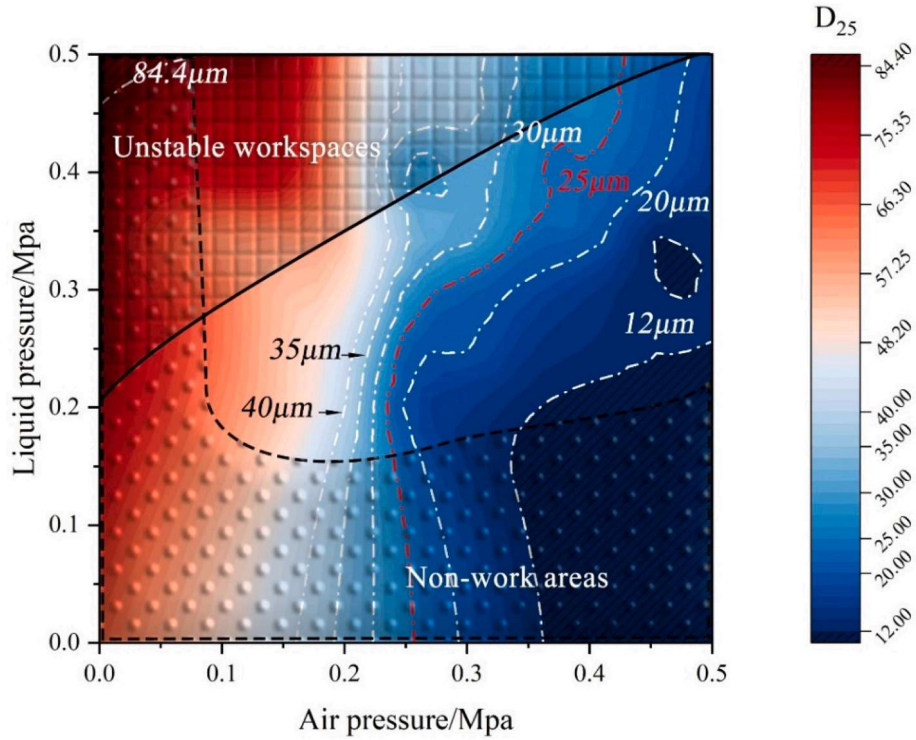
Fig. 24. D$_{25}$ contour map.

of 0.3 MPa. With constant liquid pressure, the atomization angle gradually decreases as the air pressure increases. When the air pressure is 0, a liquid column can be observed, indicating that no atomization occurs in the absence of mixed air in the liquid. Fig. 19 shows the atomization angle image collected under a constant air pressure of 0.3 MPa. As the liquid pressure gradually increases, the atomization angle also gradually increases. When the liquid pressure is 0.1 MPa and 0.15 MPa, only a small amount of liquid is sprayed out, which is due to the higher air pressure hindering the liquid from entering the mixing chamber. Fig. 20 shows the atomization angle image collected when the air and liquid pressures are equal. As the pressure increases, the atomization angle gradually increases, and when it exceeds 0.3 MPa, the atomization angle tends to stabilize at around 20°.

The experimental values of air and liquid pressure and atomization angle were fitted by a binary polynomial, and equation (9) was obtained.

$$\theta = 15.38 - 84.74P_l + 101.5P_a + 72.72P_l^2 + 13.04P_aP_l - 99.31P_a^2 \quad (9)$$

The model was validated with five sets of experimental data, and the fitting and validation goodness of fit are shown in the Table 7. The R^2 is 0.9558, indicating a good fit of the data. During the fitting process, the atomization angle of 0 was excluded to improve the fitting degree of the model. Fig. 21(a) shows the fitting diagram, and Fig. 21(b) shows the residual diagram. As can be seen from the figures, after excluding the 0 values, the residual of the edge data remained within a small range. The established polynomial model can accurately predict the atomization angle under different air and liquid pressures, and in combination with equation (5), can achieve the prediction of the ideal pollination distance.

3.3. Droplet of pollen suspension size distribution

Through the use of a laser particle size analyzer to detect the sprayed droplets in pollen fluid, differential and cumulative distributions of droplets were obtained under different air–liquid pressures. Fig. 22 shows the effect of liquid pressure on droplet distribution at a air

pressure of 0.3 MPa. It can be observed that as the liquid pressure increases, the peak of the cumulative distribution curve of droplets shifts to the left, and the D$_{25}$ value gradually increases. At the same time, the proportion of small droplets decreases significantly while the proportion of large droplets increases gradually. Fig. 23 shows the effect of air pressure on droplet distribution at a liquid pressure of 0.3 MPa. As the air pressure increases, the peak of the cumulative distribution curve of droplets shifts to the right, and the D$_{25}$ value gradually decreases. The increase in air pressure improves atomization while the increase in liquid pressure reduces atomization, mainly because the air–liquid pressure affects the air–liquid mixing ratio. When the air flow rate increases, the air–liquid laminar velocity increases, thereby increasing the rate of liquid film rupture. Table 8 shows the statistical values of D$_{25}$ under different air–liquid pressures, and the contour map of D$_{25}$ is drawn based on these data, as shown in Fig. 24. The red dotted line represents the contour line of 25 μm, and the contour lines of 20 μm, 30 μm, 35 μm, 40 μm, and the contour lines of the limit values are also drawn. In this experiment, in order to ensured that the pollen was fully enveloped by the liquid droplets, 35 μm was chosen as the threshold value. At the same time, it could be observed from the figure that in some areas, the contour lines were arranged closely together, indicating the sensitivity of this method to gas pressure. In order to ensure precise droplet size in subsequent experiments, it was necessary to accurately adjust the gas pressure. This ensured that the diameter of the droplets remained within the desired range. The unstable working range and the non-working range were also depicted on the graph. To ensure the control accuracy of pollen fluid and reduce pollen damage, the pressure range of air and liquid was determined by the black solid line, black dashed line, and the contour line of 35 μm.

3.4. Pollen plane deposition distribution

Based on the working range determined by Fig. 25, eight test points were selected for the experiment of planar pollen deposition distribution, and the experimental results were plotted on a polar coordinate axis to obtain a pollen deposition distribution cloud map. The outer
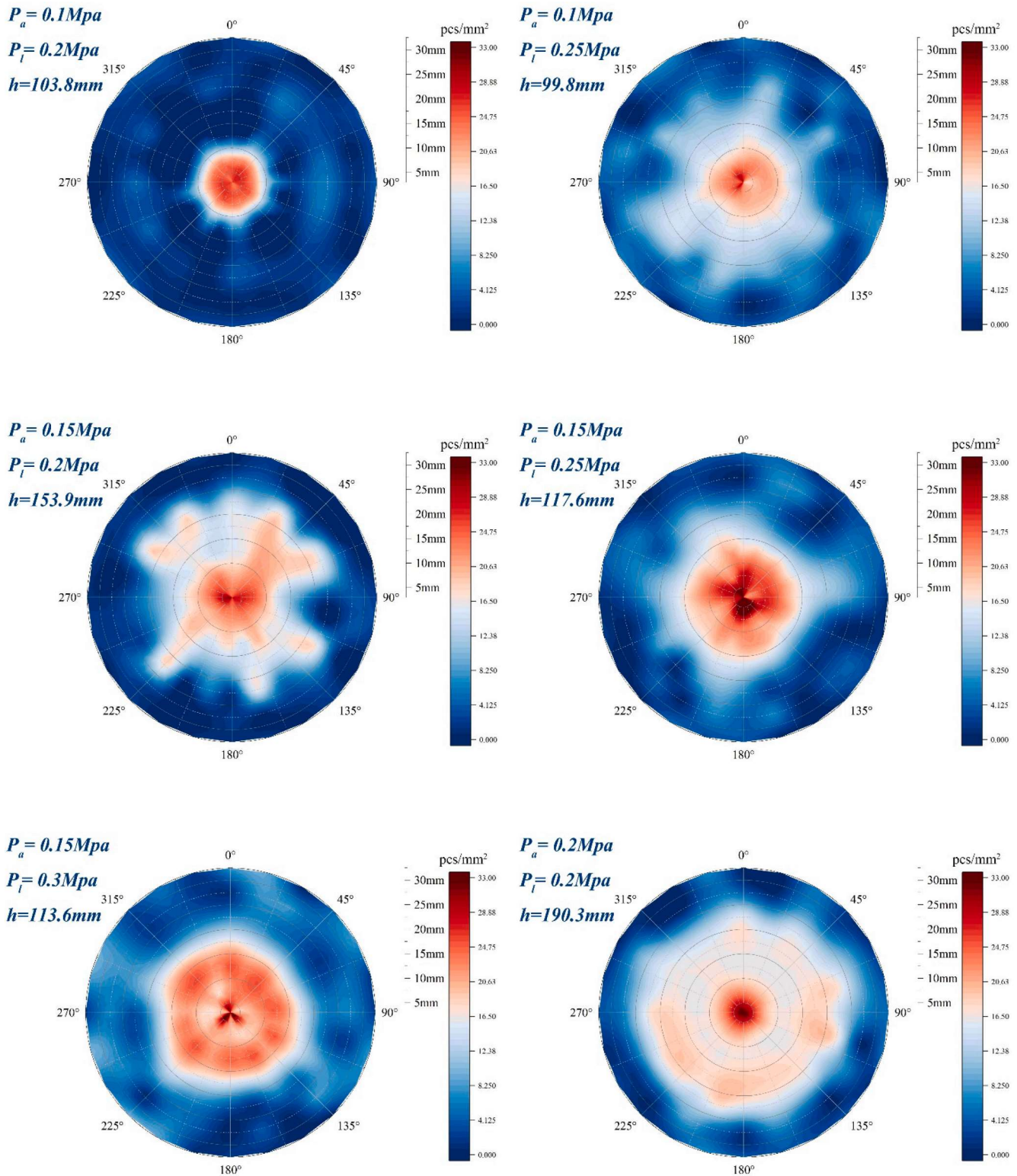
Fig. 25. Pollen plate distribution map.

edges of all eight cloud maps were presented in dark blue, indicating that there was almost no pollen distribution in the edge area. The maximum and minimum values of pollination distance were 190.3 mm and 99.8 mm, respectively, but the pollen distribution was almost concentrated in the range of the diameter D_a, indicating that the pollination distance model established in the second section could play a better role. The center positions of all cloud maps presented high-density pollen distribution, with the maximum value of 33 grains per square millimeter, indicating that the precision liquid pollinator established has a certain degree of targeting ability. When the pollination distance increases, the red high-density areas will be evenly dispersed, mainly because when the atomization angle is small, the liquid distribution
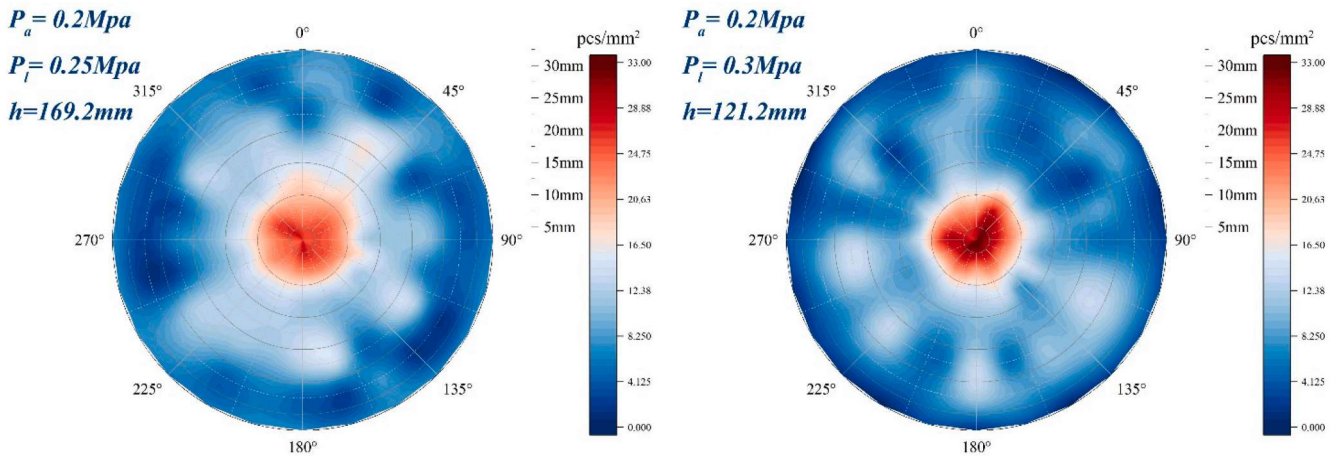
Fig. 25. (*continued*).

Table 9
Statistical results of pollen deposition under different experimental conditions.

Air pressure /MPa	Liquid pressure /MPa	Pollination distance /mm	Number of pollen deposits /pcs	Total deposition rate	Φ45 deposition rate	Φ25 deposition rate
0.1	0.2	103.8	34,128	25.86%	23.04%	21.06%
0.1	0.25	99.8	49,765	37.70%	31.76%	27.04%
0.15	0.2	153.9	48,654	36.86%	34.54%	28.27%
0.15	0.25	117.6	55,090	41.74%	37.02%	33.48%
0.15	0.3	113.6	53,942	40.87%	33.02%	29.52%
0.2	0.2	190.3	56,158	42.54%	36.62%	27.23%
0.2	0.25	169.2	59,589	45.14%	35.60%	29.41%
0.2	0.3	121.2	53,666	40.66%	33.24%	27.78%

inside the fog cone is more uniform. When the value point is closer to the 35 μm contour line, the blue area will be significantly reduced, and the white area will increase, indicating that the pollen distribution is more uniform at this time. The pollen deposition quantity and deposition rate under different experimental conditions are shown in Table 9. The theoretical quantity of pollen sprayed in this experiment was 132,000 grains. When the air pressure was 0.2 MPa and the liquid pressure was 0.25 MPa, the maximum deposition quantity reached 59,589 grains, and the overall pollen deposition rate was 45.14%. When the air pressure was 0.15 MPa and the liquid pressure was 0.25 MPa, the deposition rate in the stamen area reached the maximum value, and the deposition rates in the circular area surrounded by 45 mm and 25 mm were 37.02% and 33.48%, respectively. From the experimental results, it is observed that when the value point was closer to the 35 μm contour line, the fog droplet velocity was faster, the targeting ability was better, and the overall pollen deposition rate was significantly improved. At that time, the uniformity of the fog droplet distribution was also improved, and the pollen was more uniformly distributed in the target area, resulting in an overall increase in the pollen deposition rate. However, the pollen deposition quantity in the stamen area decreased. Therefore, for the precision liquid pollinator constructed in this study, besides focusing on the overall pollen deposition rate, the deposition rate in the stamen area should have also been considered when selecting the optimal working parameters. The air pressure of 0.15 MPa and the liquid pressure of 0.25 MPa were identified as the ideal working parameters.

3.5. Result of kiwifruit pollination verification

The pollination experiment of kiwifruit specimens was conducted using the optimal four-section stamen region deposition parameters, with an air pressure of 0.15 MPa and a liquid pressure of 0.25 MPa. The pollen deposition rate obtained was 21.15%, which was significantly lower than the 33.48% obtained by the flat plate experiment. The main reason for this decline was the significant shaking of the kiwifruit

flowers during the pollination process due to the airflow, causing some pollen suspension to deviate from the designated area, resulting in a reduced pollen deposition rate. Considering the impact of wind during actual pollination, the pollen deposition rate may be further reduced.

4. Conclusions

The following conclusions were obtained within the context of this study, where a precision liquid pollinator for kiwifruit, suitable for the end-execution part of autonomous pollination robots, was developed.

1) Grating measurement of pneumatic hydraulic cylinder stroke can achieve precise control of pollen suspension under high pressure and low flow rate. By optimizing the pollen suspension volume control, the liquid error can be controlled within $\pm$ 4.7 μl in a certain pressure range, which is an effective technical means to improve the accuracy of kiwifruit pollination. The accuracy of grating linear measurement has certain prospects in agricultural production.
2) In this study, the device working range was locked in a specific range by measuring the stable control range of the liquid, the angle of atomization variation, and the droplet size distribution range. By establishing pollen suspension volume control model and pollination distance prediction model, multiple variables were transformed into functions of air–liquid pressure, reducing the complexity of subsequent experimental design. This method provides ideas for the development and optimization of pollination devices.
3) Reducing droplet size can enhance overall pollen deposition rate. In a windless laboratory environment, the developed pollinator achieved a pollen deposition efficiency of 21.15% under an air pressure of 0.15 MPa and liquid pressure of 0.25 MPa.
4) The pollinator developed can be applied not only for kiwifruit pollination but also for plants that require liquid pollination, such as pears and apples. The evaluation method established enables a quick assessment of the pollination effectiveness of the pollinator in a

laboratory setting, providing valuable data before field experiments, thus reducing the development cycle of the pollinator.

This study has some limitations, and there are some new directions worth exploring in combination with this study. Specifically:

(1) The pollen depositio'n situation in pollination under laboratory conditions was only considered in this research, and the influence of wind on pollination was not taken into account. In the future, the precision liquid pollination device needs to be loaded onto pollination robots for field experiments to evaluate the pollination effect based on fruit set rate.

(2) In the scope of this research, it was assumed that atomized particle size smaller than 35 μm would cause damage to pollen without experimental verification. Meanwhile, it is also a question worth exploring whether liquid pressure and air–liquid pressure will cause damage to pollen.

(3) The pollination device constructed lacks an automatic filling structure, which should be considered in practical applications. The use of vacuum generators to produce negative pressure and extract pollen suspension through one-way valves will be a technology to be explored in the future.

CRediT authorship contribution statement

Wei Hao: Conceptualization, Methodology, Software, Writing – original draft, Writing – review & editing, Data curation, Visualization. **Xinting Ding:** Validation, Data curation. **Zhi He:** Methodology, Software. **Kai Li:** Investigation, Formal analysis. **Weixin Gong:** Investigation, Formal analysis. **Zixu Li:** Investigation. **Zhen Yang:** Validation. **Yongjie Cui:** Conceptualization, Writing – review & editing, Supervision, Project administration, Funding acquisition.

Declaration of Competing Interest

The authors declare that they have no known competing financial interests or personal relationships that could have appeared to influence the work reported in this paper.

Data availability

Data will be made available on request.

Acknowledgments

References

Abreu, I., Oliveira, M., 2004. Fruit production in kiwifruit (Actinidia deliciosa) using preserved pollen. Australian J. Agric. Res. 55, 565–569. https://doi.org/10.1071/AR03211.

Broussard, M.A., Goodwin, M., McBrydie, H.M., Evans, L.J., Pattemore, D.E., 2021. Pollination requirements of kiwifruit (Actinidia chinensis Planch.) differ between cultivars 'Hayward' and 'Zesy002'. New Zealand J. Crop Horticultural Sci. 49 (1), 30–40. https://doi.org/10.1080/01140671.2020.1861032.

Broussard, M.A., Howlett, B.G., Evans, L.J., McBrydie, H., Cutting, B.T., Read, S.F.J., Pattemore, D.E., 2022. Pollinator identity and behavior affect pollination in kiwifruit (Actinidia chinensis Planch.). PeerJ 10, e12963.

Castro, H., Siopa, C., Casais, V., Castro, M., Loureiro, J., Gaspar, H., Castro, S., 2021. Pollination as a key management tool in crop production: Kiwifruit orchards as a study case. Scientia Horticulturae 290, 110533. https://doi.org/10.1016/j.scienta.2021.110533.

Chang, R., Qu, X., Shi, F., 2022. Targeted deposition of kiwifruit pollen grains based on fog droplet size control. J. Northwest A&F Univ. (Natural Science Edition) 01, 1–9. https://doi.org/10.13207/j.cnki.jnwafu.2023.01.015.

Chechetka, S.A., Yu, Y., Tange, M., Miyako, E., 2017. Materially Engineered Artificial Pollinators. Chem 2 (2), 224–239. https://doi.org/10.1016/j.chempr.2017.01.008.

Cheung, A.Y., Wu, H., 2008. Structural and Signaling Networks for the Polar Cell Growth Machinery in Pollen Tubes. Ann. Rev. Plant Biol. 59 (1), 547–572. https://doi.org/10.1146/annurev.arplant.59.032607.092921.

Fan, T.-F., Park, S., Shi, Q., Zhang, X., Liu, Q., Song, Y., Chin, H., Ibrahim, M.S.B., Mokrzecka, N., Yang, Y., Li, H., Song, J., Suresh, S., Cho, N.-J., 2020. Transformation of hard pollen into soft matter. Nat. Commun. 11 (1) https://doi.org/10.1038/s41467-020-15294-w.

Ferguson, A.R., 2015. Kiwifruit in the Word - 2014. Acta Horticulturae 1096, 33–46. https://doi.org/10.17660/actahortic.2015.1096.1.

Gonzalez, M.V., Coque, M., Herrero, M., 1998. Influence of pollination systems on fruit set and fruit quality in kiwifruit (Actinidia deliciosa). Ann. Appl. Biol. 132 (2), 349–355. https://doi.org/10.1111/j.1744-7348.1998.tb05210.x.

Halbritter H. 2016. Actinidia chinensis. In: PalDat - A palynological database. https://www.paldat.org/pub/Actinidia_chinensis/301370;jsessionid=C394287332895E4029E680184008A53E. accessed 2023-04-04.

Hopping, M.E., Hacking, N.J.A., 1983. A comparison of application method for the artificial pollination of kiwifruit. Acta Horticulturae 139, 41–50. https://doi.org/10.17660/actahortic.1983.139.5.

Huang, H. (2016). Kiwifruit: The Genus Actinidia Vol. 350 (p. 1). Beijing: Science Press.

Jerram, E.M., 1979. Pollination of kiwifruit (Actinidia chinensis Planch.): Stigma-style structure and pollen tube growth. New Zealand Journal of Botany 17 (3), 233–240. https://doi.org/10.1080/0028825x.1979.10426897.

Kumari, M., Prasad, A., Rahman, L. ur, Mathur, A. K., & Mathur, A. (2022). In vitro germination, storage and microscopic studies of pollen grains of four Ocimum species. Industrial Crops and Products, 177, 114445. https://doi.org/10.1016/j.indcrop.2021.114445.

Li, K., Huo, Y., Liu, Y., Shi, Y., He, Z., Cui, Y., 2022a. Design of a lightweight robotic arm for kiwifruit pollination. Comput. Electron. Agric. 198, 107114 https://doi.org/10.1016/j.compag.2022.107114.

Li, X.-W., Li, J.-Q., 2010. A Review of the Infrageneric Taxonomy and Nomenclature of Actinidia(Actinidiaceae). Annales Botanici Fennici 47 (2), 106–108. https://doi.org/10.5735/085.047.0202.

Li, K., Zhai, L., Pan, H., Shi, Y., Ding, X., Cui, Y., 2022b. Identification of the operating position and orientation of a robotic kiwifruit pollinator. Biosyst. Eng. 222, 29–44. https://doi.org/10.1016/j.biosystemseng.2022.07.014.

Ohi, N., Lassak, K., Watson, R., Strader, J., Du, Y., Yang, C., Hedrick, G., Nguyen, J., Harper, S., Reynolds, D., Kilic, C., Hikes, J., Mills, S., Castle, C., Buzzo, B., Waterland, N., Gross, J., Park, Y.-L., Li, X., & Gu, Y. (2018). Design of an Autonomous Precision Pollination Robot. 2018 IEEE/RSJ International Conference on Intelligent Robots and Systems (IROS). https://doi.org/10.1109/iros.2018.8594444.

Pozo, M.I., Vendeville, J., Kay, C., Wackers, F., 2018. Entomovectoring technology in kiwifruit pollination. Acta Horticulturae 1218, 381–390. https://doi.org/10.17660/actahortic.2018.1218.53.

Razeto, B., Reginato, G., Larraín, A., 2005. Hand and Machine Pollination of Kiwifruit. Int. J. Fruit Sci. 5 (2), 37–44. https://doi.org/10.1300/j492v05n02_05.

Shi, F., Jiang, Z., Ma, C., Zhu, Y., Liu, Z., 2019. Controlled Parameters of Targeted Pollination Depositionby Air-Liquid Nozzle. Trans. Chinese Soc. Agric. Mach. 50 (12), 115–124. https://doi.org/10.6041/j.issn.1000-1298.2019.12.013.

Steinhorst, L., Kudla, J., 2013. Calcium - a central regulator of pollen germination and tube growth. Biochimica et Biophysica Acta (BBA) - Molecular. Cell Res. 1833 (7), 1573–1581. https://doi.org/10.1016/j.bbamcr.2012.10.009.

Strader, J., Yang, C., Gu, Y., Nguyen, J., Tatsch, C., Du, Y., Lassak, K., Buzzo, B., Watson, R., Cerbone, H., & Ohi, N. (2019). Flower Interaction Subsystem for a Precision Pollination Robot. 2019 IEEE/RSJ International Conference on Intelligent Robots and Systems (IROS). https://doi.org/10.1109/iros40897.2019.8967752.

Tacconi, G., Michelotti, V., Cacioppo, O., Vittone, G., 2016. Kiwifruit pollination: the interaction between pollen quality, pollination systems and flowering stage. J. Berry Res. 6 (4), 417–426. https://doi.org/10.3233/jbr-160138.

Tushabe, D., Rosbakh, S., 2021. A Compendium of in vitro Germination Media for Pollen Research. Front. Plant Sci. 12, 709945 https://doi.org/10.3389/fpls.2021.709945.

UN Food & Agriculture Organization (2021). Production of kiwifruit by regions. https://www.fao.org/faostat/en/#data/QCL. Accessed 2023-2-10.

Vasil, I., 1987. Physiology and Culture of Pollen. Int. Rev. Cytol. 107, 127–174. https://doi.org/10.1016/s0074-7696(08)61075-x.

Wang, Q., Lu, L., Wu, X., Li, Y., Lin, J., 2003. Boron influences pollen germination and pollen tube growth in Picea meyeri. Tree Physiol. 23 (5), 345–351. https://doi.org/10.1093/treephys/23.5.345.

Wang, P., Shi, Y., Zhang, L., Li, Y., 2019. Effect of structural parameters on atomization characteristics and dust reduction performance of internal-mixing air-assisted atomizer nozzle. Process Saf. Environm. Protect. 128, 316–328. https://doi.org/10.1016/j.psep.2019.06.014.

Wang, R., Zhang, B., Xu, R., Xing, M., Zhang, H., Zhang, H., Yan, G., Wu, H., 2022. Sensitivity of Atomization Characteristic to Operation Conditions for Air-assisted Atomizers in Snow-makers. Int. J. Refriger. https://doi.org/10.1016/j.ijrefrig.2022.12.016.

Williams, H., Nejati, M., Hussein, S., Penhall, N., Lim, J.Y., Jones, M.H., Bell, J., Ahn, H. S., Bradley, S., Schaare, P., Martinsen, P., Alomar, M., Patel, P., Seabright, M., Duke, M., Scarfe, A., MacDonald, B., 2019. Autonomous pollination of individual

kiwifruit flowers: Toward a robotic kiwifruit pollinator. J. Field Robot. 37 (2), 246–262. https://doi.org/10.1002/rob.21861.

Williams, H., Bell, J., Nejati, M., Hussein, S., Penhall, N., Lim, J., Jones, M., Ahn, H.S., Bradley, S., Schaare, P., Martinsen, P., Broussard, M., Seabright, M., Duke, M., Scarfe, A., MacDonald, B., 2021. Evaluating the quality of kiwifruit pollinated with an autonomous robot. Field Robot. 1 (1), 231–252. https://doi.org/10.55417/fr.2021009.

Wu, Q.Y., Qi, C.J., Cheng, Y.J., Cai, L.H., Zeng, Y.L., 2021. Analysis of the Impact of the COVID-19 Pandemic on Global Kiwifruit Trade. J. Fruit Sci. 38 (10), 1790–1801. https://doi.org/10.13925/j.cnki.gsxb.20210080.

Yang, X., Miyako, E., 2020. Soap Bubble Pollination. iScience 23 (6), 101188. https://doi.org/10.1016/j.isci.2020.101188.